Available online at www.sciencedirect.com

ScienceDirect

Geochimica et Cosmochimica Acta 283 (2020) 222–242

Geochimica et Cosmochimica Acta

www.elsevier.com/locate/gca

Solubility, diffusivity, and O isotope systematics of H_2O in rhyolitic glass in hydrothermal temperature experiments

Michael R. Hudak *, Ilya N. Bindeman

Department of Earth Sciences, 1272 University of Oregon, Eugene, OR 97403, United States

Received 8 October 2019; accepted in revised form 7 June 2020; Available online 17 June 2020

Abstract

In many volcanic settings, eruptive deposits experience prolonged cooling in the presence of water, such as in subglacial or submarine eruptions. Under these conditions, volcanic glass will rehydrate and record the isotopic composition of the water. This isotope exchange is moderated by H_2O solubility and diffusivity in the glass. In this study, we report results from glass hydration experiments conducted at 175–375 °C to constrain H_2O solubility and diffusivity under these hydrothermal conditions over timescales lasting hours to months. We use anhydrous high and low silica rhyolites as well as hydrous high silica rhyolite (perlites) with isotopically labeled water as starting materials. Measurements of bulk H_2O by TC/EA of experimental glasses provide minimum H_2O solubility estimates. High-Si rhyolitic glass has an H_2O solubility between 2.75 wt.% (175 °C, 0.89 MPa) and 4.1 wt.% (375 °C, 21 MPa) while low-Si rhyolite H_2O solubility is uniformly ~0.5 wt.% higher at each temperature. We find a roughly linear relationship of solubility vs 1/T that is ~1–2 wt.% greater than extrapolations from magmatic temperature solubility relationships. Furthermore, three independent methods of diffusion modeling – one in situ and two mass balance approaches – all produce H_2O diffusivity (D_{H2O}) values that up to 5.5 times greater than predicted by extrapolation of the 1/T – D_{H2O} relationships above 400 °C to the experimental P-T-X_{H2O} conditions. In situ H_2O profiles in rhyolite particles measured by NanoSIMS have the characteristic "snowplow " functional form that arises from the H_2O concentration dependence of D_{H2O}. We cannot detect diffusively driven kinetic fractionation of D relative to H with the NanoSIMS data. Diffusion and mass balance calculations that fit TC/EA time series of bulk H_2O in particles of a single size distribution, and calculations that reconcile two sets of different sized particles at a single experimental duration, return similar D_{H2O} constraints. We also present time series $\delta^{18}O$ of bulk glass ($\delta^{18}O_{bulk}$) and the $\delta^{18}O$ of water-in-glass ($\delta^{18}O_{wig}$) measurements, which indicate that molecular water (H_2O_m) dissolved in the glass is the primary driver of subsequent oxygen isotope exchange between glass and an external fluid. Local equilibrium between the $\delta^{18}O_{wig}$ and the $\delta^{18}O_{bulk}$ is rapidly established and ranges from approximately −14‰ at 175 °C to −10‰ at 375 °C. Both the $\delta^{18}O_{bulk}$ and $\delta^{18}O_{wig}$ then increase with time moving slowly towards estimated bulk glass $\delta^{18}O$ equilibrium with the external experimental water. Oxygen isotope exchange between glass and a fluid is therefore strongly linked to – and is limited by – H_2O diffusivity, which is slower at lower P-T conditions and lower H_2O solubilities as H_2O_m diffusion is the main exchange mechanism.

Keywords: Rhyolite; Glass; Hydration; Diffusivity; Solubility; Hydrothermal; Oxygen isotopes

1. INTRODUCTION

Water in volcanic glasses and melts has long been recognized as an important tool for understanding magmatic and volcanic processes, igneous phase equilibria, and timescales

* Corresponding author.
E-mail address: mhudak2@uoregon.edu (M.R. Hudak).

https://doi.org/10.1016/j.gca.2020.06.009
0016-7037/

of volcanic and post-eruptive processes. The physical properties of hydrous melts are well understood in nature and experiments largely because the devolatilization of magma, which is dominated by the exsolution of H_2O in silicic systems, is a primary driver of eruptions and their explosivity (e.g. Sparks, 1978; Eichelberger and Westrich, 1981). The solubility of H_2O in a melt is function of pressure, temperature, and to a lesser degree, the concentrations of other volatile species, namely CO_2 (e.g. Newman and Lowenstern, 2002; Liu et al., 2005). These variables have been constrained by a large number of high- and low-pressure experiments to constrain pre-eruptive storage conditions and degassing behavior in a magmatic conduit (e.g. Zhang et al., 1991; Zhang and Behrens, 2000; Ni and Zhang, 2008). Diffusivity of water in high-temperature systems is especially important for understanding formation and growth of bubbles and subsequent degassing in volcanic conduits because it limits how rapidly H_2O can diffuse out of the melt and into bubbles (Watkins et al., 2012), which can additionally be used as a geospeedometer (Zhang et al., 1997, 2007; Wilding et al., 1995; Xu and Zhang, 2002).

At Earth surface temperatures, rehydration (also referred to as secondary hydration) of felsic volcanic glasses has significantly different applications, although correcting for rehydration has allowed for more robust interpretations of volcanic processes. Rehydration of volcanic glass occurs on long timescales that do not make it readily amenable for even years-long experiments to constrain diffusivity, solubility, glass stability, or isotope exchange. There are a few exceptions that rely on the extremely high resolution of ion microprobe depth profiling of experimental and tephrochronologically constrained obsidians, which provides high spatial resolution to resolve micron-length profiles (Anovitz et al., 2004, 2008, 2009; Riciputi et al., 2002). Otherwise, carefully selected natural samples of known age have been the primary method for evaluating D_{H2O} over a range of glass compositions (e.g. Friedman and Smith, 1960; Friedman et al., 1993b, 1993a; Seligman et al., 2016). These results enable hydration rind thicknesses in obsidian to be used as a proxy for the age of archeological artifact, with the rate of hydration as a function of time or $t^{0.5}$ (e.g. Michels et al., 1983; Liritzis and Laskaris, 2011). In other studies, bulk analytical approaches have also been attempted in long-term (months to years) hydration experiments of thin-walled volcanic ash with isotopically labeled H_2O to assess isotope exchange (Nolan and Bindeman, 2013; Cassel and Breecker, 2017). Ratios of D/H in volcanic glasses have been employed to estimate the D/H ratios of paleo-meteoric waters at the time of pyroclast emplacement as a proxy for paleoaltitude (Cassel et al., 2009, 2012, 2014; Canavan et al., 2014; Dettinger and Quade, 2015; Jackson et al., 2019) and paleoclimate (Colwyn and Hren, 2019).

Few studies have targeted an intermediate temperature range between Earth surface temperatures and ~400 °C, which we refer to as "hydorthermal" for simplicity, appropriate for cooling ignimbrites and lavas or for the formation of perlites (Friedman et al., 1966; Keating, 2005; Bindeman and Lowenstern, 2016; Randolph-Flagg et al., 2017; Hudak and Bindeman, 2018; Seligman et al., 2018). The dynamics of volcanic glass hydration below the glass transition temperature (T_g), the temperature at which silicate melts begin to exhibit more brittle (~400 °C), glass-like behavior (e.g. Dingwell and Webb, 1990; Dingwell, 1995; Hess and Dingwell, 1996) are less well understood for two primary reasons. First, most materials cool and pass through this temperature range relatively quickly. Second, prolonged time at these temperatures induced glass breakdown to secondary alteration products (e.g. clays and zeolites; Cullen et al., 2019). Additionally, in regimes with very slow cooling, vitreous ignimbrites devitrify and grow crystallites and spherulites (Watkins et al., 2009; Gardner et al., 2012; Breitkreuz, 2013; von Aulock et al., 2013; Befus et al., 2015). However, hydrothermal glass hydration occurs in a number of settings including in subglacial (Wilding et al., 2000; Stroncik and Schmincke, 2001; Thien et al., 2015) or submarine eruptions (e.g. Mitchell et al., 2018) and cooling ignimbrites (Keating, 2005; Randolph-Flagg et al., 2017; Hudak and Bindeman, 2018; Seligman et al., 2018) and plays a critical role in the formation of perlite (Friedman et al., 1966; von Aulock et al., 2013; Bindeman and Lowenstern, 2016). Hydrothermal hydration experiments can provide constrains on H_2O diffusivity and solubility that can aid in interpreting the volatile record of glasses from these settings. Experiments can also help inform both the interpretation of a new oxygen isotope tool that measures the $\delta^{18}O$ of that water-in-glass ($\delta^{18}O_{wig}$) that excludes silicate-bound oxygen, and the mechanism of oxygen isotope exchange between glass or rhyolite and water.

In this study, we experimentally investigate the dynamics of glass hydration and the behavior of water in glass over a range of hydrothermal temperature conditions that all glasses pass through during the cooling. We evaluate the extent to which well-constrained relationships between temperature, H_2O solubility, and D_{H2O} can be extrapolated below the glass transition. Furthermore, we seek to understand how oxygen isotopes exchange both between glass and an external fluid and within the glass between the silicate and the water dissolved in glass.

2. EXPERIMENTAL METHODS

2.1. Experimental materials and material preparation

Three obsidians were used in the hydration experiments, two of which are anhydrous and one that has been naturally rehydrated. The first anhydrous glass (0.08 wt.% H_2O), and the main glass used in all experiments, comes from a low silica rhyolite (LSR) obsidian flow at Newberry volcano, Oregon, USA. (Common abbreviations and notations are provided in Table 1.) Feldspar phenocrysts are rare (<5%) and the obsidian is relatively microlite-poor (Manga, 1998). Electron probe microanalysis (EPMA) give a mean glass SiO_2 of 71.45 wt.% (0.72 wt.%, 1σ) while total alkalis ($Na_2O + K_2O$) are relatively high at 11.15 wt.% (0.39 wt.%, 1σ). Major element concentrations of starting materials and ratios of non-bridging oxygen to tetrahedrally coordinated cations (NBO/T), which provide struc-

Table 1
Definitions of common variables and abbreviations in order of appearance in text.

Abbreviation	Definition
TC/EA	High temperature conversion elemental analyzer
D_{H2O}	diffusivity of H_2O in glass
$\delta^{18}O_{bulk}$	measured bulk $\delta^{18}O$ composition (‰$_{VSMOW}$)
wig	water-in-glass; H_2O dissovled in glass either as undegassed magmatic H_2O or secondary H_2O from rehydration in the environment
$\delta^{18}O_{wig}$	measured $\delta^{18}O$ composition of the water-in-glass (‰$_{VSMOW}$)
H_2O_m	molecular H_2O
$\alpha_{glass\text{-}wig}$	equilibrium fractionation factor between bulk glass and internal water-in-glass, expressed as ratio of isotopes in glass divided by the ratio of isotopes in H_2O (R_{glass}/R_{H2O})
$10^3 ln\alpha_{glass\text{-}wig}$	approx. equilibrium fractionation factor between bulk glass and internal water-in-glass (‰$_{VSMOW}$)
LSR	low silica rhyolite experimental glass; from Newberry volcano, OR, USA
EPMA	Electron probe microanalyzer
NBO/T	ratio of non-bridging oxygens to tetrahedrally coordinated cations; a proxy for the degree of polymerization of a melt or glass with lower numbers indicating greater degrees of polymerization
r_{eff}	effective radius of oblate ellipsoid particles
HSR	high silica rhyolite experimental glass; from Yellowstone, WY, USA
NanoSIMS	nano-secondary ion mass spectroscopy; high spacial resolution SIMS
H_2O_{bulk}	bulk H_2O; same as H_2O_t, but specific to a bulk measurement of H_2O or the modeled for a whole particle
H_2O_t	total H_2O, including H_2O_m and OH; herein used for conc. at a single point in a sample or node in a model
$\alpha_{glass\text{-}H2O}$	equilibrium fractionation factor between bulk glass and external H_2O, expressed as ratio of isotopes in glass divided by the ratio of isotopes in H_2O (R_{glass}/R_{H2O})
$10^3 ln\alpha_{glass\text{-}H2O}$	approx. equilibrium fractionation factor between bulk glass and external H_2O (‰$_{VSMOW}$)
$\alpha_{rhyolite\text{-}H2O}$	equilibrium fractionation factor between rhyolite and external H_2O, expressed as ratio of isotopes in glass divided by the ratio of isotopes in H_2O ($R_{rhyolite}/R_{H2O}$)
$10^3 ln\alpha_{rhyolite\text{-}H2O}$	approx. equilibrium fractionation factor between rhyolite and external H_2O (‰$_{VSMOW}$)
$\alpha_{wig\text{-}H2O}$	equilibrium fractionation factor between internal water-in-glass and H_2O external to the glass, expressed as ratio of isotopes in glass divided by the ratio of isotopes in H_2O (R_{glass}/R_{H2O})
$10^3 ln\alpha_{wig\text{-}H2O}$	approx. equilibrium fractionation factor between internal water-in-glass and H_2O external to the glass (‰$_{VSMOW}$)
C_{sat}	saturation concentration of H_2O applied to the surface of the glass in diffusion models; meant to reflect H_2O solubility
$\delta^{18}O_{sil}$	calculated $\delta^{18}O$ composition the silicate component of the glass (‰$_{VSMOW}$); excludes contributions from water-in-glass

tural information about the degrees of polymerization, are given in Tables A.1-A.3.

Four particle size fractions were used over the course of the experiments. Particle sizes for abraded LSR glasses were determined using a Microtrac PartAn3D particle size analyzer that gives mean particle dimensions and the calculated effective radius (r_{eff}) of each batch of particles (Trafton et al., 2019; Appendix B). At 225 °C and 375 °C, a single size fraction of rounded particles with an effective radius (r_{eff}) of 160 μm were used. At 175 °C, three particle sizes were used. Two were rounded and have r_{eff} of 95 μm and 155 μm. The third set of particles were not abraded, but sieved to a size fraction of 53–105 μm, which corresponded to the maximum dimension of the intermediate axis diameter. (In figures, this is given as r = 26–53 μm for comparison to the measured and modeled effective radii of larger particle size.) A later set of experiments at 225 °C use these three size fractions, once most of the 160 μm radius particles were consumed. At 275 °C, the abraded particles with r_{eff} of 95 μm and 155 μm were used. (Particle sizes are given in Table 2.)

The second anhydrous rhyolite is a high silica rhyolite (HSR) from the Summit Lake flow at Yellowstone, USA (0.15 wt.% H_2O). The glass has 75.11 wt.% SiO_2 (0.51 wt. %, 1σ) and 9.52 wt.% alkalis (0.22 wt.%, 1σ; Table A.4). The Summit Lake flow has 3–6% crystallinity dominated by quartz and feldspar (Loewen et al., 2017), and these were avoided during by hand-picking glass under a microscope. This glass was only used for experiments at 225 °C because of the more limited amount of material available and because it more or less duplicates the major element chemistry of the Nez Perce perlitic rhyolite. Particle size distributions were not made prior to the experiments, so an effective radius is not given.

The third rhyolitic glass comes from the Nez Perce flow which, like the Summit Lake glass, is a rhyolite from the Central Plateau in Yellowstone. This glass is a perlite, a rehydrated high-Si rhyolite glass (76.02 ± 0.54 wt.% SiO_2, 1σ) that is used to assess isotopic exchange between glass and water through time. This perlitic material has onion skin-like, curvilinear fractures with higher water "skins" around central less hydrous spherical cores. The skins naturally separate, sloughing off the obsidian cores as a result of rapid hydration and volume change (Fig. 1). Perlite cores and skins have identical major element compositions within 1σ when normalized on an anhydrous basis. Skins and cores are relatively uniform in size and shape and were not sieved. Perlite skins have shorter dimensions (10 s of μm) than the perlite cores (100 s of μm). Perlite cores having lower H_2O than the hydration rinds or outer skins, both in

Table 2
Particle size distribution data and calculated effective radii of low-Si anhydrous rhyolitic glass. The effective radii (r_{eff}) are determined by comparing the volume % of experimental glass particles with the mean particle length (l), width (w), and height (h) data (oblate ellipsoid geometry) to the volume % of spheres that remained anhydrous as a function of radius.

Sieve fraction 105–500 μm										
Analysis	*# of particles*	*Mean l/2 (μm)*	*1σ (μm)*	*Mean w/2 (μm)*	*1σ (μm)*	*Mean h/2 (μm)*	*1σ (μm)*	*Mean of radii (μm)*	*2σ (μm)*	r_{eff} *(μm)*
1	2366	242	138	179	77	114	64	178	160–162	
Sieve fraction 250–350 μm										
Analysis	*# of particles*	*Mean w/2 (μm)*	*2σ (μm)*	*Mean l/2 (μm)*	*2σ (μm)*	*Mean h/2 (μm)*	*2σ (μm)*	*Mean of radii (μm)*	*2σ (μm)*	r_{eff} *(μm)*
1	18,791	181	70	285	163	96	54	187	149–154	
2	19,620	183	77	293	177	96	54	191	151–155	
3	19,601	183	76	291	177	96	54	190	150–155	
Total	58,012	182	75	290	173	96	54	189	150–155	
Sieve fraction 105–250 μm										
Analysis	*# of particles*	*Mean l/2 (μm)*	*2σ (μm)*	*Mean w/2 (μm)*	*2σ (μm)*	*Mean h/2 (μm)*	*2σ (μm)*	*Mean of radii (μm)*	*2σ (μm)*	r_{eff} *(μm)*
1	3337	174	175	94	103	65	50	111	91–95	
2	3476	168	156	93	97	68	53	110	92–95	
3	3104	164	165	90	98	66	52	107	89–93	
Total	9917	169	165	92	99	66	52	109	90–95	

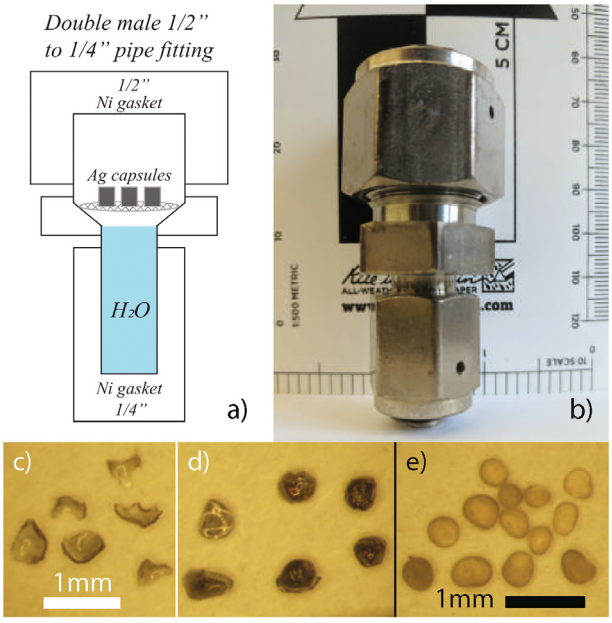

Fig. 1. Schematic (a) and photo (b) of the experimental vessels for glass hydration by water vapor and the experimental materials (c-e). High-Si perlites are separated into skins (c) and cores (d). Note the rims on the cores are likely skins that have not broken off. Abraded LSR particles were sieved to several size fractions including 250–350 μm (e) for experiments. The white and black scale bars correspond to (c,d) and (e), respectively.

their H_2O_{bulk} measurements (<0.75 wt.% vs. ≥ 2 wt.%) and spot analyses of total H_2O (H_2O_t; <0.5 wt.% vs. ≥ 1.5 wt.%; Bindeman and Lowenstern, 2016). Crystallinity is low (<5%) and a population of pyroxene microlites exists but does not appear to affect hydration of the glass.

Two waters were used in the hydration experiments. The first and primary H_2O used in the experiments is an isotopically-labeled mixture of water used in earlier hydration experiments (Nolan and Bindeman, 2013) and Fiji Water®. The very high $\delta^{18}O$ values (+56‰) of the H_2O in the Nolan and Bindeman (2013) was useful for their slower, lower T experiments, but was too heavy to be used directly in these experiments in case the glasses approached the $\delta^{18}O$ of the experimental H_2O and required large extrapolations beyond our silicate standards. Fiji Water® is an internal laboratory standard with known compositions for H and O isotopes that allowed us to design a mixture with target $\delta^{18}O$ and δD compositions. The experimental water was analyzed at IsoLab at the University of Washington on a Picarro L2120i cavity ringdown spectrometer (Table A.5). Samples were measured in duplicate, with each duplicate consisting of a set of 10 analyses, the first 5 of which are discarded to avoid memory effects. Means of $\delta^{18}O$ are (5.93 ± 0.09)‰ and (5.83 ± 0.04)‰, and means of δD are (74.97 ± 1.42)‰ and (76.17 ± 2.22)‰ (errors are 2σ). We use the mean of these duplicate analyses: 5.88‰ $\delta^{18}O$ and 75.6‰ δD. The second experimental H_2O is a mixture of H_2O and D_2O in an approximately 1:1 ratio, which is used specifically for the NanoSIMS diffusion profile measurements. Combinations of water, glasses, and glass size fractions used in the experiments are given in Table 3.

Table 3
Experimental materials, conditions, and durations for reported hydration results. Nolan-Fiji water refers to a mixture of high δD and $\delta^{18}O$ (reported in Nolan and Bindeman, 2013) and a internal laboratory standard (FIJI Water®). Deuterated water refers to a 1:1 mixture of D_2O and H_2O, which was used only for NanoSIMS work.

Experiment	*Glass*	*Water*	*Size Fraction (μm)*	*T (°C)*	*Time (hours)*
2	LSR	Nolan-Fiji	105–500	225	167
3	LSR	Nolan-Fiji	105–500	225	4, 24
3	HSR	Nolan-Fiji	not sieved, <1500	225	4, 24, 116
3	Perlite skins	Nolan-Fiji	N/A	225	4, 24, 116
3	Perlite cores	Nolan-Fiji	not sieved, <1000	225	4, 24, 116
3b	LSR	Nolan-Fiji	105–500	225	240, 423
3b	HSR	Nolan-Fiji	105–1500	225	356, 539
3b	Perlite skins	Nolan-Fiji	N/A	225	356, 539
3b	Perlite cores	Nolan-Fiji	not sieved, <1000	225	356, 539
4	LSR	Deuterated	250–350	225	334
5	LSR	Nolan-Fiji	105–1000	375	12, 24, 36, 42, 48
5	Perlite skins	Nolan-Fiji	N/A	375	12, 24, 36, 42, 48
5	Perlite cores	Nolan-Fiji	not sieved, <1000	375	12, 24, 36, 42, 48
8	LSR	Nolan-Fiji	105–250	175	935, 3000, 6000
8	LSR	Nolan-Fiji	250–350	175	935, 3000, 6000
8	LSR	Nolan-Fiji	350–500	175	935, 3000, 6000
8	Perlite skins	Nolan-Fiji	N/A	175	935, 3000, 6000
8	Perlite cores	Nolan-Fiji	not sieved, <1000	175	935, 3000, 6000
10	LSR	Nolan-Fiji	53–105	225	1010
10	LSR	Nolan-Fiji	105–250	225	1010
10	LSR	Nolan-Fiji	250–350	225	1010
10	Perlite skins + cores	Nolan-Fiji	not sieved, <1000	225	1010
13	LSR	Nolan-Fiji	53–105	275	12, 24, 96, 192
13	LSR	Nolan-Fiji	105–250	275	12, 24, 96, 192
13	LSR	Nolan-Fiji	250–350	275	12, 24, 96, 192

2.2. Experimental design

The experimental vessel is fashioned out of a double male stainless-steel fitting that is ½" on one end and ¼" (12.7 mm and 6.35 mm, respectively) on the other end and sealed with nickel gaskets (Fig. 1). Within the fitting, there is a beveled rim at the transition between the two widths. It has a volume of 2.3 cm^3 when sealed. Experiments were run for hours to months at 175 °C, 225 °C, 275 °C and 375 °C. Vessels were loaded with 0.36 mL of experimental H_2O for 175 °C, 225 °C, and 375 °C experiments; and 0.40 mL were loaded for the 275 °C experiments. This volume of water greatly exceeds the mass of water that can diffuse into a few tens of mg of glass, so it may be considered an infinite reservoir that would not change in isotopic composition for the duration of the experiment.

The vessel was oriented with the ¼" side down. Stainless-steel mesh was placed on the bevel to suspend the samples above the liquid water. The silver capsules loaded with glass were placed on the mesh and the vessel was sealed with Ni gaskets. A muffle furnace was pre-heated to the desired temperature and the vessels were placed inside. Fractionations between liquid and vapor phases are corrected for the O isotope compositions of the hydrating H_2O vapor are given in Table A.6 and are calculated using Horita and Wesolowski (1994). When extractions of glass were made from the experiments after cooling to room temperature, the experimental water was removed and replaced with new experimental H_2O in case of H_2O loss and/or fractionation during the extraction.

3. ANALYTICAL METHODS

Total H_2O, bulk $\delta^{18}O$, and water-in-glass $\delta^{18}O$ measurements were conducted on a gas source MAT 253 isotope ratio mass spectrometer (IRMS). Experimental glasses dried between 110 and 150 °C for at least 1 hour in a vacuum oven and no longer than overnight to remove any adsorped water before they were weighed and loading for analysis. This drying method successfully reproduces H_2O concentrations measured by manometry or Fourier-transform infrared spectroscopy (Martin et al., 2017). For bulk H_2O and $\delta^{18}O_{wig}$ analyses, 1–4 mg of glass were weighted on a high precision balance with 0.002 mg precision for masses <10 mg and loaded into Ag foil capsules and sealed. Samples and standards were dried overnight at between 110–150 °C in a vacuum over to ensure any adsorbed water was removed.

Analyses of H_2O_{bulk} and $\delta^{18}O$ of water-in-glass ($\delta^{18}O_{wig}$) were conducted with a high temperature conversion elemental analyzer (TC/EA) interfaced with the MAT 253 IRMS. Samples were introduced into the TC/EA down a

glassy carbon tube inside a furnace at 1450 °C. Upon melting, volatiles in the sample are liberated where they react with the glassy carbon in a pyrolysis reaction that generates H_2 and CO gas. These gases are transported to an open split by a He carrier gas. A reference gas of known composition is also introduced into the open split to monitor instrument stability. Both the sample gas and the reference gas are introduced to the IRMS from the open split. Separate analytical sessions for H_2 and CO were conducted for bulk H_2O and $\delta^{18}O_{wig}$, respectively. Mica standards USGS57 (biotite) has 3.60 wt.% H_2O and is used for H_2O_{bulk} calibration. It is analyzed 3–5 times throughout each analytical session for H_2O. In 9 analytical sessions, the 2σ on this standard never exceeded 0.20 wt.% H_2O. This error is within the 6% 2σ reproducibility that Martin et al., (2017) report for samples >3 wt.% H_2O_{bulk}. The $\delta^{18}O_{wig}$ data are calibrated with USGS water standards (W-62001, VSMOW, USGS-47, and USGS-53). Despite the reductive environment, no detectible oxygen is given off for the silicates. Additionally, fractionation of $\delta^{18}O$ is <1‰ between oxygen in water-in-glass and oxygen structurally bound in the glass silicate the during thermal decomposition and simultaneous pyrolysis (Seligman and Bindeman, 2019). See Seligman and Bindeman (2019) for further $\delta^{18}O_{wig}$ methods and discussion. The limited amount of experimental glass removed at each extraction only permitted one H_2O_{bulk} and one $\delta^{18}O_{wig}$ analysis. Therefore, we use the maximum 2σ (0.20 wt.%) for H_2O_{bulk} in the USGS57 biotite standard from the 9 H_2O_t analytical sessions. Water standards used to calibrate $\delta^{18}O_{wig}$ have lower errors than solid samples. Therefore, we take the maximum 1σ (1.5‰) $\delta^{18}O_{wig}$ error reported for rhyolitic and dacitic glasses measured by Seligman and Bindeman (2019) as a conservative instrumental error.

Bulk $\delta^{18}O$ measurements are made on 1–2 mg of material fluorinated by BrF_5 and using a 9.6 μm CO_2 laser, with a chamber connected to a line connected to the MAT 253 IRMS. The laser chamber is pretreated with BrF_5 reagent until acceptable blanks (<0.1 μmol) are achieved. Sample yields are typically within 15–25 μmol. Samples are introduced in single blocks from the 12-sample turret, which is hosted in a custom-built vacuum airlock chamber. This prevents premature mass loss in reactive samples during reaction of the glass with BrF_5 during pretreatment of the laser chamber. Samples are converted to a gas by a laser in the presence of BrF_5. The sample gas is purified by a series of liquid nitrogen traps and a Hg diffusion pump to separate the O_2. The O_2 is converted to CO_2 by a carbon rod before being introduced to the mass spectrometer for analysis. Samples were analyzed and normalized with 2–4 Gore Mountain garnet standards (UOG) in each of the 4 analytical sessions. As with the TC/EA H_2O_{bulk} sessions, limited sample material prevented duplicate analysis and 1σ is taken from the standard measurements, which is ≤0.1‰ for 3 of the sessions. The standards in the session for 175 °C experimental glasses yielded a 1σ of 0.27‰. Isotope compositions are expressed in delta notation relative to Vienna Standard Mean Ocean Water (VSMOW). Oxygen isotope data is presented in delta notation according to Eq. (1) for both bulk $\delta^{18}O$ and $\delta^{18}O_{wig}$.

$$\delta^{18}O = \left({}^{18/16}O_{sample} / {}^{18/16}O_{VSMOW} - 1\right) \times 1000 \quad (1)$$

The diffusion profiles of H and D in a low-Si rhyolite glass were acquired with a Cameca NanoSIMS 50L ion microprobe at Caltech. A 40-spot line scan with a ~2 μm step was measured perpendicularly to the glass surface. On each spot, an 8 keV Cs^+ primary beam of ~100 nm in size (~20 pA) was used to sputter the sample in a 1 × 1 μm rastering mode. Secondary ions (H^- and D^-) of −8 keV were simultaneously collected with electron multipliers (EMs). A pre-sputtering of 60 sec was applied to get rid of the gold coating and surface contamination. To avoid edge effects, secondary signals were only collected from the center 0.8 × 0.8 μm of the 1 × 1 μm crater with electronic gating. The total data acquisition time on each spot was about ~400 sec (200 frame X 2.048 sec/frame). The mass resolving power (MRP) at the EM detector for D^- was >2000, more than enough to resolve D^- from any possible H_2^- interference. Electron microprobe data were collected on a Cameca SX100 at the University of Oregon using a 15 kV beam running at 15 nA for Na, K, Si, Al, Fe, Mg, Ca, and Ti. The alkalis were analyzed first, followed by Si and Al. A time-dependent intensity (TDI) correction was applied to these elements. EPMA analyses were calibrated with a set of 13 standard. Five high purity (>99.98%) synthetic oxides (MnO, SiO2, TiO2, MgO, and NiO) and 2 synthetic NIST glasses (K-411 and K-412) were used along with mineral specimens including a synthetic forsterite, synthetic chloroapatite, nepheline, diopside, orthoclase, and magnetite.

4. RESULTS

4.1. Bulk H_2O concentrations in glass

The 175 °C experiments utilized three particle sieve fractions of LSR glass: 250–350 μm, 105–250 μm, and 53–105 μm. The larger two size fractions were abraded and have effective radii (r_{eff}) of approximately 155 and 95 μm, respectively (Appendix B). All three sizes show increases in H_2O (Fig. 2a) with time, reaching H_2O_{bulk} concentrations of 0.65, 1.03, and 2.75 wt.% H_2O_t (from largest to smallest) by the end of the 6000 hour-long experiment. This contrasts the Nez Perce perlite skins, which dehydrate from initial H_2O_{bulk} contents of 2.89 wt.%. The perlite skins lose ~0.15–0.2 wt.% and do not fully recover to their initial bulk H_2O content. The perlite cores increase to 2.64 wt.% H_2O_{bulk}, approaching the H_2O_{bulk} of the perlite skins after 6000 hours. This experiment allows us to constrain the solubility of H_2O in this high silica glass at 175 °C to ~2.75 wt %. By the end of the experiment at 6000 hours, the smallest LSR particles catches up to the perlite bulk H_2O concentrations at 2.75 wt.%.

At 225 °C, both LSR and HSR show similar bulk H_2O trends that increase relatively linearly through time at 225 °C (Fig. 2b). The largest LSR particle size in the 1010 hour-long experiment (r_{eff} = 155 μm) is roughly comparable to the particle sizes of the initial set of experiments and continues the linear bulk H_2O trend (r_{eff} = 160 μm). The smallest size fraction has the highest H_2O_{bulk} concentration (3.70

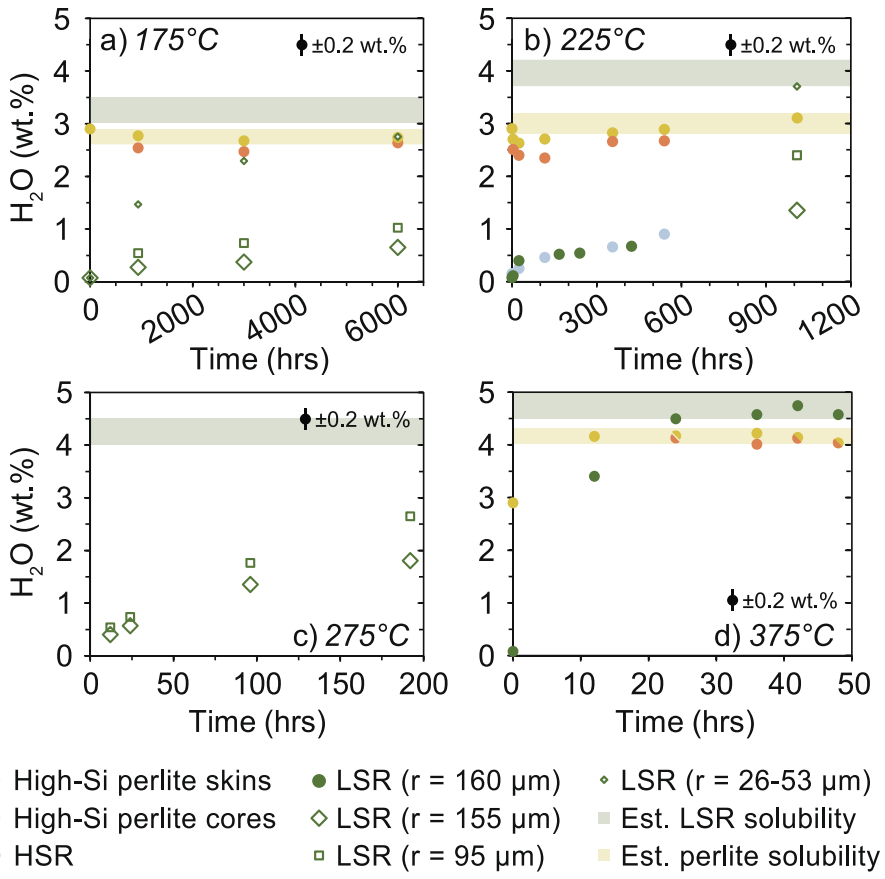

Fig. 2. Bulk H_2O TC/EA measurements from experiments at 175 °C (a), 225 °C (b), 275 °C (c), and 375 °C (b). In all experiments, all anhydrous glasses (HSR and LSR) increase in H_2O with time while perlites dehydrate slightly at 175 °C, dehydrate and then recover at 225 °C, and increase in H_2O at 175 °C. Error bars indicate 2σ reproducibility of standards.

wt.%) and the largest size fraction has the lowest concentration (1.35 wt.%) in the 1010 hour-long experiment. Hand-picked perlite skins and cores remain around 3.0–3.1 wt.% H_2O through time, although they both show evidence for dehydrating initially before recovering. Zones within the perlite with H_2O_t greater than H_2O solubility will dehydrate faster than zones of lower H_2O_t will hydrate because of the H_2O concentration dependence of D_{H2O}., which may cause H_2O_{bulk} to decrease before recovering. This indicates that H_2O solubility in low silica rhyolitic glass at 225 °C and 2.55 MPa is no less than, and perhaps a few tenths of wt.% higher than the maximum measured H_2O_{bulk} of 3.7 wt.%. The H_2O solubility is slightly lower for high silica rhyolite, around 3.1 wt.% H_2O_{bulk} based on the plateau in the times series (Fig. 2b).

Hydration occurs much more quickly above 250 °C. In the 275 °C experiments, only the intermediate (r_{eff} = 95 µm) and large (r_{eff} = 155 µm) LSR glasses were used. The intermediate particle size shows more rapid hydration than the large particles, reaching 2.65 wt.% H_2O_{bulk} after 192 hours while the larger particles have 1.80 wt.% bulk H_2O after the same amount of time (Fig. 2c). After 192 hours, the particles began sintering and developed an opaque coating, so the experiment was terminated.

Water content in the LSR glass increased rapidly in the 375 °C experiments and plateaued around 4.6 wt.% H_2O_{bulk} by 24 hours at 375 °C (Fig. 2d). The LSR glass (r_{eff} = 160 µm) peaks at 42 hours at 4.75 wt.%, but at all other durations after 12 hours, remains between 4.50–4.57 wt.% H_2O_{bulk}. The perlites skins and cores also reached higher water contents within 24 hours but are somewhat lower than the initially anhydrous glass at ~4.1 wt.% in each time interval, with a maximum concentration in the skins at 36 hours with 4.22 wt.% H_2O.

In summary, our experiments showed that low-Si rhyolite has higher H_2O solubility than high-Si rhyolite, likely by ~0.5 wt.% H_2O. The smallest LSR particles and the hydrous high-Si perlites, which should most rapidly approach the limit of H_2O solubility in rhyolitic glass, appear to record increasing solubility with increasing pressure and temperature.

4.2. Oxygen isotope compositions

4.2.1. Bulk $\delta^{18}O$ of glass

The bulk $\delta^{18}O$ results at 175 °C and 225 °C show little change in the low-Si anhydrous glasses and gradual change in the high-Si hydrous perlites (Fig. 3a,b; Table 4). The LSR obsidian, does not deviate more than ~0.3‰ in

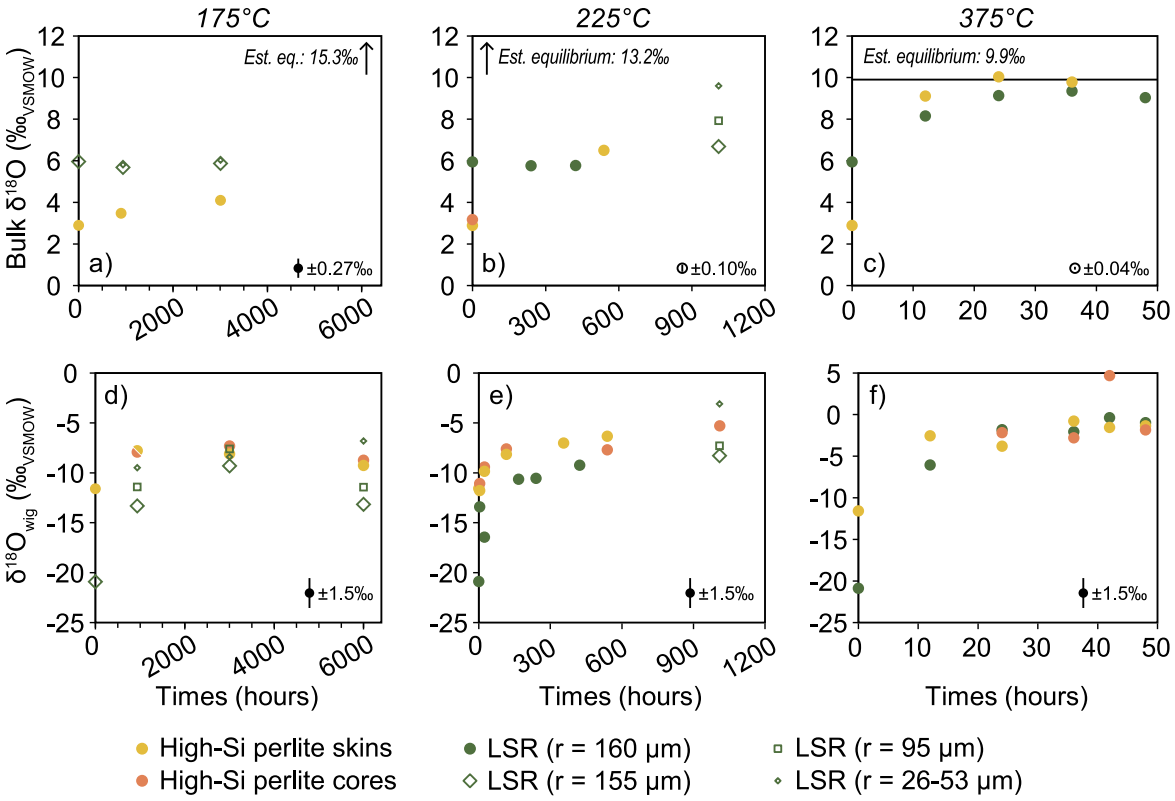

Fig. 3. Bulk $\delta^{18}O$ (a-c) and $\delta^{18}O_{wig}$ (d-f) measurements from experiments at 175 °C (a,d), 225 °C (b,e), and 375 °C (c,f). Bulk $\delta^{18}O$ does not change as much at 175 °C or 225 °C as it does in 375 °C where hydration is complete, and the glass achieves equilibrium with the H_2O. The $\delta^{18}O_{wig}$ (d-f) approaches a plateau at all temperatures, suggesting that local equilibrium within the glass has been achieved. Equilibrium $\delta^{18}O$ of the glass is predicted by combining the $10^3\ln\alpha_{albite\text{-}H2O}$ (O'Neil and Taylor, 1967) and $10^3\ln\alpha_{quartz\text{-}H2O}$ (Sharp et al., 2016) in the eutectic proportions of albite and quartz in rhyolite.

$\delta^{18}O_{bulk}$ from the initial starting composition of 5.95‰, even after 3000 hours. In contrast, the initially hydrous perlites (2.89 wt.%) increased by 1.2‰ $\delta^{18}O_{bulk}$ over the same interval (Fig. 3a). The difference in behavior between smallest LSR glasses and the thin high-Si perlite skins suggests that for significant oxygen isotope exchange to occur between glass and water, the glass must first be hydrated. Incomplete hydration at 175 °C therefore limits the extent to which the $\delta^{18}O$ of the bulk glass can be modified after 3000 hours.

The data from the 225 °C experiments record the same $\delta^{18}O$ behavior as observed in the 175 °C experiments, in which the high-Si perlites steadily increase with time while the LSR obsidian is slow to change. The perlites increased by 5‰ from 2.89‰ to 7.93‰ $\delta^{18}O_{bulk}$ in 1010 hours at a nearly linear rate, whereas the intermediate sized LSR particles have increased by <1‰ from 5.95‰ to 6.69‰ $\delta^{18}O_{bulk}$ (Fig. 3b). The smallest particle size of LSR glass reached a $\delta^{18}O_{bulk}$ value of 9.60‰ after 1010 hours, which is greater than the perlite $\delta^{18}O_{bulk}$. While higher in $\delta^{18}O$ than the perlites, the relative change from the initial $\delta^{18}O$ of the two glasses is less in the LSR glass relative to the perlites, so this higher $\delta^{18}O$ does not necessarily represent more significant exchange. However, given the bulk H_2O content of 3.7 wt.% and the short diffusion length scales required, the smallest LSR particles may be fully hydrated allowing for more rapid $\delta^{18}O$ exchange between glass and water.

If the oxygen isotope compositions of the experimental glasses are dominantly controlled by the extent of hydration, then only completely hydrated glasses will record a $\delta^{18}O$ composition in equilibrium with the fluid. In this case, equilibrium is only attained in the 375 °C experiments where there is evidence for complete hydration halfway through the duration of the experiment from the plateau in bulk H_2O. At this temperature with a $\delta^{18}O$ of +5.88‰ fluid, elevated glass $\delta^{18}O_{bulk}$ values of +9 to +10‰ are achieved within 24 hours in both the LSR glasses and high-Si perlites and subsequently plateau (Fig. 3c). This gives an equilibrium oxygen isotope fractionation between glass and H_2O ($10^3\ln\alpha_{glass\text{-}H2O}$) of 3-4‰ between glass and water at 375 °C, and is consistent with predicted rhyolite-H_2O fractionation ($10^3\ln\alpha_{rhyolite\text{-}H2O}$) of 4.04‰ using equilibrium $\delta^{18}O$ fractionation factors for albite-H_2O (O'Neil and Taylor, 1967) and quartz-H_2O (Sharp et al., 2016) in their eutectic proportions (2:1; Bindeman and Lowenstern, 2016; Hudak and Bindeman, 2018). Our data validates that that this simple quartz and albite approximation for rhyolite $\delta^{18}O$ fractionation is appropriate to use in the hydrothermal temperature window in which we conduct these experiments.

Table 4
Total H_2O and $\delta^{18}O$ data for expermental glasses (LSR, HSR, and perlites skins and cores) as a function of time. Errors for $\delta^{18}O_{bulk}$ come from standard 1σ (n = 2–4) for that analytical session. See methods section for discussion of $\delta^{18}O_{bulk}$ and H_2O error. [a]The smallest particle sizes could not be measured, so the range of radii given is half the lengths of the sieve fraction size range for these particles (53–105 μm).

Material	*Effective radius (μm)*	*Duration (hours)*	*H_2O (wt.%)*	*$\delta^{18}O_{wig}$ (‰)*	*$\delta^{18}O_{bulk}$ (‰)*	*$\delta^{18}O_{bulk}$ 1σ (‰)*
Initial Experimental Glass Compositions						
LSR	n/a	0	0.08	−20.9	5.95	0.10
HSR	n/a	0	0.15	−4.9		
Perlite skins	n/a	0	2.90	−11.6	2.89	0.10
175 °C Experimental Results						
LSR	155	935	0.28	−13.3	5.67	0.27
LSR	155	3000	0.38	−9.3	5.86	0.27
LSR	155	6000	0.65	−13.2		
LSR	95	935	0.55	−11.4		
LSR	95	3000	0.74	−7.6		
LSR	95	6000	1.03	−11.4		
LSR	26-53[a]	935	1.47	−9.5	5.80	0.27
LSR	26-53[a]	3000	2.29	−8.4	6.02	0.27
LSR	26-53[a]	6000	2.75	−6.8		
Perlite skins	n/a	935	2.77	−7.8	3.47	0.27
Perlite skins	n/a	3000	2.68	−8.1	4.09	0.27
Perlite skins	n/a	6000	2.74	−9.3		
Perlite cores	n/a	935	2.54	−7.9		
Perlite cores	n/a	3000	2.47	−7.3		
Perlite cores	n/a	6000	2.64			
225 °C Experimental Results						
LSR	n/a	0	0.08		5.95	0.10
LSR	160	4	0.20	−13.4		
LSR	160	24	0.40	−16.4		
LSR	160	167	0.52	−10.6		
LSR	160	240	0.54	−10.6	5.76	0.10
LSR	160	423	0.67	−9.2	5.77	0.10
LSR	155	1010	1.35	−3.1		
LSR	95	1010	2.40	−7.3	6.69	0.10
LSR	26-53[a]	1010	3.70	−8.3	9.60	0.09
HSR	n/a	4	0.15	−11.6		
HSR	n/a	24	0.25	−8.2		
HSR	n/a	116	0.46	−9.4		
HSR	n/a	356	0.66	−7.8		
HSR	n/a	539	0.90	−9.9		
Perlite skins	n/a	4	2.70	−11.8	2.89	0.10
Perlite skins	n/a	24	2.63	−9.8		
Perlite skins	n/a	116	2.71	−8.1		
Perlite skins	n/a	356	2.82	−7.0		
Perlite skins	n/a	539	2.89	−6.3	6.50	0.10
Perlite cores	n/a	4	2.51	−11.1		
Perlite cores	n/a	24	2.40	−9.4		
Perlite cores	n/a	116	2.34	−7.6		
Perlite cores	n/a	356	2.66			
Perlite cores	n/a	539	2.67	−7.7		
Perlite cores	n/a	1010	3.10	−5.3	7.93	0.09
275 °C Experimental Results						
LSR	155	12	0.40			
LSR	155	24	0.57			
LSR	155	96	1.35	−4.0		
LSR	155	192	1.80	−1.4		
LSR	95	12	0.54			
LSR	95	24	0.74			
LSR	95	96	1.77	−2.3		
LSR	95	192	2.65	4.5	7.46	0.09

375 °C Experimental Results						
LSR	160	12	3.40	−6.1	8.16	0.04
LSR	160	24	4.50	−1.8	9.13	0.04
LSR	160	36	4.57	−2.0	9.35	0.04
LSR	160	42	4.75	−0.4		
LSR	160	48	4.57	−1.0	9.04	0.04
Perlite skins	n/a	12	4.16	−2.5	9.11	0.04
Perlite skins	n/a	24	4.17	−3.8	10.04	0.04
Perlite skins	n/a	36	4.22	−0.8	9.79	0.04
Perlite skins	n/a	42	4.14	−1.5		
Perlite skins	n/a	48	4.03	−1.3		
Perlite cores	n/a	24	4.13	−2.2		
Perlite cores	n/a	36	4.02	−2.8		
Perlite cores	n/a	42	4.12	4.7		
Perlite cores	n/a	48	4.04	−1.8		

4.2.2. $\delta^{18}O$ of water-in-glass

We employ a rarely reported parameter that can shed light on oxygen isotope systematics called the $\delta^{18}O$ of water-in-glass, or $\delta^{18}O_{wig}$, which represents the H_2O-bound oxygen atoms within the hydrous glasses (Bindeman and Lowenstern, 2016; Hudak and Bindeman, 2018; Seligman and Bindeman, 2019). Oxygen that is structurally bonded in the silicate does not contribute to this parameter, even in redox-sensitive Fe-silicates (Seligman and Bindeman, 2019). At all temperatures, $\delta^{18}O_{wig}$ increases with time for both low-Si anhydrous obsidian and high-Si perlites. The noisiest data comes from the 175 °C time series (Fig. 3d). All the glasses increased in $\delta^{18}O_{wig}$ until 3000 hours (except for the perlite skins which showed effectively no change between 935 and 3000 hours with a 0.3‰ decrease) and nearly all samples decreased between 3000 and 6000 hours. The only glass to increase over this final time interval, and to show constant increases through the entire experimental duration are the small LSR particles, which ended at −6.8‰ $\delta^{18}O_{wig}$. The large and intermediate sized LSR particles showed the largest decreases of nearly 4‰ to −13.2‰ and −11.4‰ $\delta^{18}O_{wig}$, respectively, −16.7‰ and −14.9‰ below the H_2O vapor composition of 3.5‰ $\delta^{18}O$. These compositions are identical to the 935 hour-long $\delta^{18}O_{wig}$ compositions. The perlite skins and cores also decreased by ~1‰ between 3000 and 6000 hours to −9.3‰ and −8.7‰ $\delta^{18}O_{wig}$, respectively.

The data from the 225 °C experimental glasses show a more consistent increase though time (Fig. 3e). At the shortest durations (≤24 hours) and lowest H_2O_{bulk} contents, the LSR $\delta^{18}O_{wig}$ are variable, but demonstrate an increase through time reaching −9.2‰ by 423 hours. Both large (r_{eff} = 155 μm) and intermediate (r_{eff} = 95 μm) LSR particle sizes at 1010 hours can be interpreted as an extension of the shorter duration LSR particles (r_{eff} = 160 μm). These achieve $\delta^{18}O_{wig}$ values of −8.3‰ and −7.3‰, respectively, after 1010 hours of hydration. The smallest LSR particles reach a maximum $\delta^{18}O_{wig}$ of −3.1‰, which is greater than any of the perlite data. The perlites have an exponential trend through time that increases quickly initially and then begins to plateau towards the end of the experimental duration. Perlite skins and cores increase together and the cores reach −5.3‰ after 1010 hours.

The glasses reach consistent $\delta^{18}O_{wig}$ values between −2.0‰ and −0.4‰ $\delta^{18}O_{wig}$ at longer durations and temperatures >250 °C. Two outliers of 4.5‰ after 192 hours at 275 °C and 4.7‰ after 42 hours at 375 °C are more than 5‰ higher than any other $\delta^{18}O_{wig}$ values at those temperatures and are therefore not considered to be representative. The 375 °C experimental glasses increase in $\delta^{18}O_{wig}$ especially quickly, with the LSR particles and the perlites attaining the same values by 24 hours and slowly increasing together within error until the end of the experiment at 48 hours (Fig. 3f). Given that the bulk H_2O content of these particles plateaued at similar timescales, suggesting complete hydration, the $\delta^{18}O_{wig}$ of the LSR particles can be interpreted to be effectively equilibrated with the $\delta^{18}O$ of the fluid of 5.9‰. Values averaging −1.2‰ for LSR and high-Si perlite skins after 36 hours suggest that the equilibrium fractionation between $\delta^{18}O_{wig}$ and the $\delta^{18}O$ of the hydration water ($10^3\ln\alpha_{wig\text{-}H2O}$) is approximately −7‰; and the $10^3\ln\alpha_{glass\text{-}wig}$ is ~11–12‰.

The $\delta^{18}O_{wig}$ data increases through time in all samples at 225 °C and 375 °C and in the smallest, highest bulk H_2O LSR particles from the 175 °C experiments. Only minor shifts in the bulk $\delta^{18}O$ occur in the 175 °C and 225 °C experiments and the $\delta^{18}O_{wig}$ tracks the bulk $\delta^{18}O$ in the 375 °C experiments. Therefore, the plateaus through time observed in the $\delta^{18}O_{wig}$ data at lower temperatures (Fig. 3d,e) alone do not provide enough information to tell if the fluid $\delta^{18}O$ composition or the glass $\delta^{18}O$ composition control the $\delta^{18}O_{wig}$.

4.3. NanoSIMS D and H profiles

One hydration experiment used a mixture of deuterated water (~99.9% D_2O) and Fairbanks tap water (δD = −152‰) in 1:1 proportions so that D and H profiles in experimental glass could be measured independently at high resolution by NanoSIMS. This experiment lasted 334 hours at 225 °C. Spots with a 1 μm diameter were collected every 1–2 μm (Fig. 4a, Appendix C). Hydrogen and deuterium

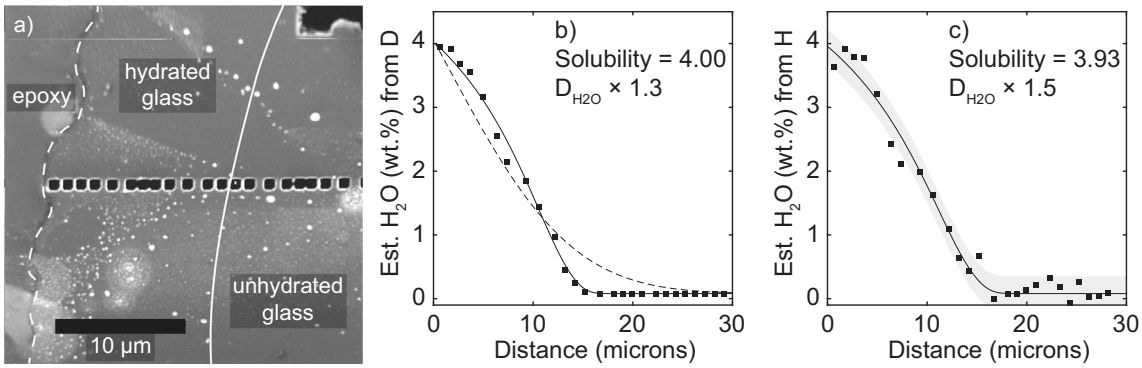

Fig. 4. NanoSIMS 0.8 × 0.8 μm measurements on LSR glass from a 334 hour-long experiment at 225 °C with half D_2O and half Fairbanks tap water (normal H_2O) spaced every 1–1.5 μm (a). The dashed line shows the edge of the glass and the solid line shows the approximate distance over which H_2O has been added to the glass. Example NanoSIMS diffusion profiles (solid curves) for D (b) and H concentrations (c) scaled to 0.08 wt.% H_2O in the interior and 3.95 wt.% at the boundary to match the diffusivity modeling. These profiles yield D_{H2O} values of 1.3 (D) and 1.5 (H) times greater than extrapolated from the Zhang and Behrens (2000) model. Best fit solubility concentrations are 4.00 and 3.93 wt.% H_2O, respectively. A constant D_{H2O} is modeled in (b; dashed line) to underscore the importance of the H_2O concentration dependence of D_{H2O}. The shaded region of (c) is 2σ of the 27 points of H background measurements beyond the diffusion front.

are measured as $^1H^+$ and $^2H^+$, respectively. Backgrounds for H are much higher than for D and H is more readily detected by SIMS than D (Anovitz et al., 2008). Once this is corrected and the D profile (in counts) were scaled to match the H profile, no difference in profile shape or diffusion profile length could be detected at this resolution. The half-fall distances – the distance at which the concentration in the diffusion profile is half the difference of the boundary and background concentrations – are at approximately 8 μm in the corrected data for both D and H and are as wide at the precision of measurement. This suggests that there is not a kinetic isotope effect resulting from faster D or H diffusion into glass. The lack of kinetic isotope effects in D/H fractionation during glass hydration is consistent with previous work (Shelby, 1977; Anovitz et al., 2008; Roskosz et al., 2018).

Hydrogen profiles yield D_{H2O} estimates that are marginally faster than those modeled for the D profiles but have slightly lower best fit solubilities for the boundary condition (see Section 5.1. for details of diffusion modeling). Some of this difference may arise from imperfect scaling of the data because the background of the H profile includes both 0.08 wt.% water in the glass and residual H_2O vapor in the vacuum chamber. We emphasize that the NanoSIMS data are semi-quantitative in terms of absolute abundances of D and H (but not in width), so the results are informative in that they constrain how D_{H2O} and H_2O solubility co-vary and in the overall length scale of H_2O diffusion. Profiles are scaled to 3.95 wt.% H_2O_t at the boundary for D (Fig. 4b), and because the boundary at the rim for the H is lower than the next two points in the profile, the second point in the H profile is arbitrarily scaled to match the second point in the D profile (Fig. 4c). The resulting H_2O solubilities for D and H are 4.00 wt.% and 3.93 wt.%, respectively. The D_{H2O} estimates for are 1.3 times greater for D and 1.5 times greater for H than predicted for the relevant P-T-X_{H2O} conditions in high temperature extrapolations of Zhang and Behrens (2000). These correspond to D_{H2O} values at glass rim (assuming the rim has H_2O_t concentrations equaling the H_2O solubility) of 8.31×10^{-13} cm^2s^{-1} for D and 9.21×10^{-13} cm^2s^{-1} for H. The dashed line in Fig. 4b represents the average of the maximum and minimum D_{H2O} values (4.303×10^{-13} cm^2s^{-1}) in a non-H_2O concentration dependent diffusion model. It returns the same mass of H_2O diffused into the glass as the H_2O concentration-dependent model but does not fit the data. Using a constant diffusivity yields a functional form of an error function as opposed the observed "snowplow" form. (We use the snowplow analogy to describe the region of high concentrations that arise near the boundary of the model as a result of the concentration dependence of D_{H2O}. This occurs when the boundary has higher concentrations of the diffusive species than the background in the rest of the model). This demonstrates that H_2O concentration dependent model is appropriate for modeling D_{H2O} in rhyolitic glasses at hydrothermal temperatures, but that constant D_{H2O} values can be used for comparison.

5. DISCUSSION

We investigate three interrelated processes – H_2O diffusivity, H_2O solubility, and $\delta^{18}O$ exchange in glass in our hydrothermal temperature experiments from 175 to 375 °C. Diffusion of molecular water in rhyolitic melts is the primary mechanism for the movement of oxygen within the silicate and this facilitates isotope exchange between external fluids and the melt (Behrens et al., 2007). Below magmatic temperatures, as we demonstrate here, H_2O_m diffusion in glass is likewise the fastest mechanism for $\delta^{18}O$ exchange between glass and a fluid. Therefore, D_{H2O} in glass should place the greatest constraint on the rate $\delta^{18}O$ exchange between glass and a fluid because self-diffusion (diffusion achieved by individual atoms changing their position with one another within a solid phase) is orders of magnitude slower. Above 400 °C, D_{H2O} in rhyolitic glasses and melts is well-constrained experimentally (Delaney and Karsten, 1982; Lapham et al., 1984; Zhang et al., 1991; Zhang and Behrens, 2000; Liu et al., 2005; Ni and Zhang, 2008). At Earth surface temperatures, many

authors have constrained D_{H2O} in glass and their data points to diffusivities largely between 10^{-17} and 10^{-19} m^2s^{-1} Anovitz et al., 2004, 2009; Giachetti et al., 2015, 2020; Friedman and Smith, 1960; Friedman and Long, 1976; Friedman and Obradovich, 1981; Yokoyama et al., 2008; Rogers and Duke, 2011; Stevenson et al., 2013).

This compilation demonstrates that D_{H2O} for surface conditions is higher than extrapolations from the high temperature data by roughly 2 orders of magnitude, although both high and low temperature trends follow an Arrhenius relationship (Fig. 5; Table D). It is imperative to understand the transitional behavior of D_{H2O} between high and low temperature regimes over the hydrothermal temperature range, which could shed light on this discrepancy. However, we note that the mechanics of diffusion in melts and glasses appears to be quite similar. Molecular water is the diffusive species in both melts (e.g. Zhang et al., 1997, 1991; Behrens et al., 2007) and in glasses at low temperature (e.g. Nolan and Bindeman, 2013; Anovitz et al., 2008). Furthermore, in both high and low temperature experiments, the functional form of the H_2O diffusion profiles have the same "snowplow" that results from the H_2O concentration dependence of D_{H2O} at high temperature.

5.1. H_2O solubility in rhyolitic glass

Hydration experiments conducted here between 175 and 375 °C and at pressures of 0.89 to 21 MPa refine H_2O solubility in glass below the glass transition (Fig. 6). Precise H_2O solubility data for silicic glasses in this hydrothermal temperature range is virtually nonexistent. Well-accepted solubility models at magmatic temperatures, constrained by experiments no lower than 400 °C, act as a primary point of comparison for the maximum bulk H_2O contents observed in this study. The results from these experiments demonstrate that both the LSR glass and the high-Si perlites are >1 wt.% more hydrated than predicted by extrapolating H_2O solubilities from VolatileCalc (Newman and Lowenstern, 2002) or Liu et al. (2005; Fig. 6). An isobaric 1 MPa curve is also shown to help consider the pressure dependence of H_2O solubility (Liu et al., 2005). This curve shows a decrease in solubility with increasing temperature, which suggests that the higher H_2O_{bulk} concentrations are likely more a function of pressure than temperature. In one experiment by Liu et al. (2005), reproducible and higher than expected H_2O concentrations are achieved and omitted from their model, which they justify by proposing that the P-T-X conditions of the experiment put it into a regime of secondary hydration (Ryan et al., 2015). While pressure surely plays a role in controlling the solubility of H_2O in rhyolitic glass, there is to date no predictive model that we are aware of that can disentangle the role of pressure and temperature below 400 °C.

Our most confident H_2O solubility estimates come from 375 °C, where all investigated glasses have achieved complete hydration, and 225 °C where the perlites have plateaued in H_2O_{bulk} and the smallest LSR particle size is likely to be completely hydrated. At 375 °C and 21 MPa, the LSR glass reaches at 4.65 ± 0.15 wt.% H_2O_{bulk} and the high-Si perlites plot round 4.12 ± 0.1 wt.% H_2O_{bulk} compared to a predicted 3.11 wt% H_2O_{bulk} at these P-T conditions from VolatileCalc (Newman and Lowenstern, 2002) and 2.79 wt.% H_2O_{bulk} from the model of Liu et al., (2005). At 225 °C and 2.55 MPa, the measured bulk H_2O concentrations exceed the high temperature model predictions (1.18 wt.% H_2O and 1.46 wt.% from Liu et al., (2005) and Newman and Lowenstern (2002), respectively) by even more than the 375 °C experimental glasses. The smallest size fraction of LSR obsidian achieves 3.70 wt.% H_2O_{bulk} after 1010 hours, which we consider to be the solubility. The relative offset of ~0.6 wt.% bulk H_2O between the LSR and the perlites is maintained at this lower temperature as the high-Si perlites do not exceed 3.10 wt.% H_2O_{bulk}.

At 175 °C or 275 °C, the LSR glasses do not achieve complete hydration at the conclusion of the experiments. Instead, the results at 225 °C and 375 °C, and an experiment from Cullen et al. (2019) at 250 °C can assist in estimating H_2O solubility at these temperatures by

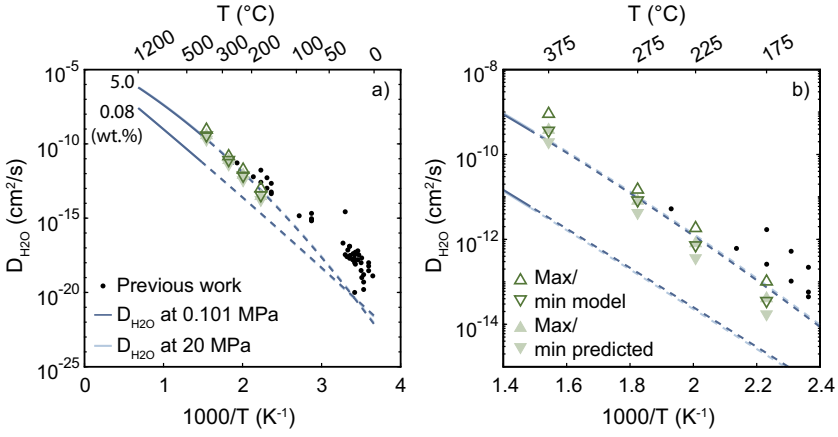

Fig. 5. Results from this study are compared to high T extrapolations for diffusivity of water in melts and glass (Zhang and Behrens, 2000) and a compilation of low T diffusivities of water in glass (a; Appendix D). High T models cannot be extrapolated to Earth surface temperatures, which are off by ~2 orders of magnitude. The high T models do better over the range of hydrothermal T (175–375 °C) in this study, remaining within a factor of 5.5 at maximum over the relevant P-T-X_{H2O} (b).

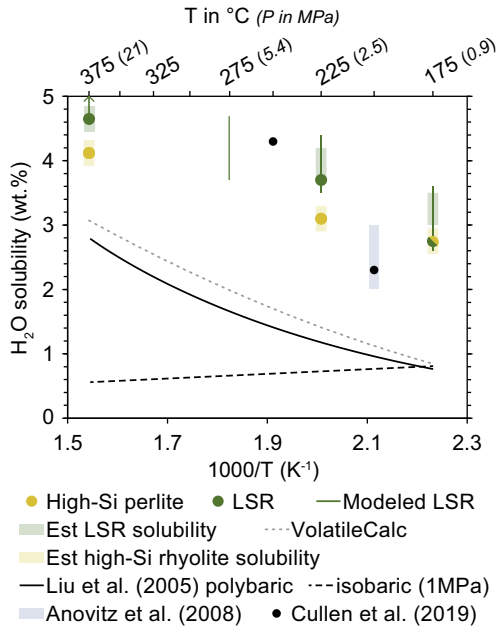

Fig. 6. Estimated H_2O solubilities (shaded) as a function of 1/T for LSR and high-Si perlites are compared to predictions from VolatileCalc (Newman and Lowenstern, 2002) and Liu et al., (2005) for the P-T conditions of the experiments and an isobaric model at 1 MPa. An estimate from Anovitz et al. (2008) and the H_2O content of 2 hydrothermal experiments from Cullen et al. (2019) are also shown. For diffusivity modeling, the range of H_2O solubilities used (green bars) is expanded by 2σ (or 0.2 wt.%) of TC/EA bulk H_2O measurements.

extrapolation. If we assume the relationship between 1/T (in Kelvin) and H_2O solubility is linear, the fit to the available H_2O data gives a possible upper limit of ~3.2–3.4 wt.% H_2O_t. The 175 °C perlites remain unchanged after 6000 hours and match the H_2O_{bulk} of the smallest LSR particles at an H_2O_{bulk} of 2.75 wt.%, suggesting that is the solubility of high-Si rhyolitic glass. Then if we apply observation of the ~0.6 wt.% offset between high-Si perlites and LSR solubility at 225 °C and 375 °C, this also gives an estimate solubility consistent with the linear 1/T-H_2O solubility fit of approximate 3.3 wt.% H_2O_{bulk}. The linear extrapolation yields an H_2O solubility estimate of ~4.1–4.3 wt.% H_2O_t at 275 °C.

This difference in H_2O solubility between the perlitic high-Si rhyolite and LSR glass is likely related to glass chemistry and/or structure. Higher silica generally correlates with higher NBO/T ratios, since Si is the dominate cation occupying tetrahedrally coordinated sites. Both silica (Friedman and Long, 1976) and the degree of polymerization recorded by lower NBO/T ratios (Behrens and Nowak, 1997; Nolan and Bindeman, 2013) have been identified as primary controls on H_2O solubility and/or diffusivity in rhyolitic melts and glasses. Other differences in major elements likely also play a role, especially alkalis which are mobile and may exchange with hydrogen or H_2O_m or during more advanced stages of alteration after hydration (e.g. Cerling et al., 1985; Friedman and Long, 1976), although we do not observe evidence for systematic alkali mobility in experimental glasses (Fig. A.7). In our experiments, the LSR has a higher NBO/T of 0.07 than either the HSR (0.035) or the perlites (0.01), primarily because of the difference in SiO_2, but also because of the much higher alkali content of the LSR (which increases NBO).

In summary, we observe H_2O solubility in high-Si perlite that is ± 0.2 wt.% of the following values: 2.75 wt.% at 175 °C, 3.1 wt.% at 225 °C, and 4.1 wt.% at 375 °C. The H_2O solubility for low silica rhyolitic glass is ± 0.3 wt.% for the lower temperature results and ± 0.2 wt.% for the 375 °C results centered around 3.3 wt.% at 175 °C, 3.9 wt.% at 225 °C, 4.2 wt.% at 275 °C, and 4.8 wt.% at 375 °C. [These error ranges are determined in part by the reproducibility of bulk H_2O on the TC/EA, which is within 6% of the bulk H_2O concentration when $H_2O_{bulk} > 3.0$ wt.% (Martin et al., 2017).] We attribute this difference in solubility to the differences in major element chemistry and any effect this may have on glass structure.

5.2. Diffusion modeling of H_2O in rhyolitic glass

To model the TC/EA bulk H_2O data and the NanoSIMS D and H profiles, we employ a 1D finite difference diffusion model in spherical coordinates and use the outputs to compute simultaneous mass balance calculations. Only LSR obsidian particles (initially 0.08 wt.% H_2O_{bulk}) are modeled because they are used in experiments at all temperatures. To adequately capture the H_2O concentration dependence of D_{H2O}, we employ the D_{H2O} model of Zhang and Behrens (2000) as a starting point (Eq. (2)). Their D_{H2O} is calibrated to experiments above 400 °C, so our model follows the approach of Seligman et al. (2016) in assuming that functionally Zhang and Behrens (2000) is correct and where the diffusivity is adapted by a constant prefactor to fit the data.

$$D_{H_2O_t} = prefactor \times Xexp(m)\left\{1+\exp\left[\begin{matrix}56+m+X\left(-34.1+\frac{44{,}620}{T}+\frac{57.3P}{T}\right)\\ -\sqrt{X}\left(0.091+\frac{4.77\times10^6}{T^2}\right)\end{matrix}\right]\right\} \quad (2)$$

Here, X is the mole fraction of H_2O_t on a single oxygen basis, $m = -20.79 - (5030/T) - (1.4P/T)$, T is temperature in Kelvin, and P is pressure in MPa. The H_2O concentration dependence of D_{H2O} gives rise to the following form of Fick's first law of diffusion in spherical coordinates (Eq. (3)).

$$\frac{\partial C}{\partial t} = \frac{2}{r}D\frac{\partial C}{\partial r} + D\frac{\partial^2 C}{\partial r^2} + \frac{\partial C}{\partial r}\frac{\partial D}{\partial r} \quad (3)$$

Here, C is the concentration of H_2O_t in mole fraction, t is time in seconds, r is the radius of the sphere in μm, and D is the modified H_2O_t concentration dependent diffusivity of Zhang and Behrens (2000) in $\mu m^2/s$. Spheres with radii of 160 μm, 155 μm, or 95 μm are used based on the size data for the various batches of abraded particles (Table 2). Each model discretizes the radius into nodes of 1 μm and the concentrations of H_2O_t at each node are weighted by their volume in a sphere to sum the mass of bulk H_2O in in the model particle at each time step (Appendix E).

5.2.1. Diffusion modeling of bulk H_2O concentrations through time

Mass balance calculations are coupled with the diffusion model and applied to the TC/EA bulk H_2O data to fit D_{H2O} over a reasonable range of H_2O solubilities at each temperature. In the following discussion of the model results, H_2O solubility is only achieved at the surface of the glass where it is assigned as the boundary condition. For clarity and to distinguish from the measured data, we refer to this boundary condition H_2O solubility in the model as the saturation concentration, or C_{sat}. Diffusivity and C_{sat} have an inverse relationship. The greater the diffusivity, the more rapidly the bulk H_2O content of the glass increases. Therefore, when diffusivity is increased, the C_{sat} boundary condition must be lowered to compensate in order to fit the measured H_2O_{bulk} time series. Examples of some of the chi-squared best fits D_{H2O} for are shown for each temperature (Fig. 7; Appendix E) but are non-unique solutions and the relationship that defines the best fit D_{H2O} as it varies with C_{sat} are shown in Fig. 8. The boundary condition corresponding to the glass-water interface uses a prescribed C_{sat} for the H_2O_t while the rest of the glass and is initially 0.08 wt.% H_2O_t with the interior boundary condition set to equal the adjacent node (in case the hydration front should reach the glass interior by the end of the model run, as it does at 375 °C). Some rhyolite hydration research suggests that H_2O surface concentrations and solubility in rhyolitic glass increases exponentially through time with progressive hydration, and on very short length scales (Anovitz et al., 2004). However, pending better verification of how H_2O solubility changes through time in our samples, our models do not take this into account. We thus only present diffusion and mass balance models that have a constant H_2O_t concentration for the boundary condition.

Unlike high temperature extrapolations of H_2O solubility, absolute D_{H2O} values solubility (Fig. 8a) and D_{H2O} prefactors of the Zhang and Behrens (2000) diffusivity equation (Fig. 8b), show only a subtle increase in H_2O diffusivity compared to extrapolations. Our diffusivity prefactors vary within half an order of magnitude of the high temperature relationships. The chi-square best fit models in Fig. 7 can explain the trends of H_2O_{bulk} in LSR obsidian through time with progressive hydration. The dashed lines represent 10% variation in the effective radius of the glass particles, which illustrate that small variation in the 1–3 mg aliquots of particles extracted from the experiments could explain much of the spread in the bulk H_2O data. The models do best at fitting the 95 μm radius particles at 175 °C (Fig. 7a) and the 160 μm radius particles 225 °C (Fig. 7b) and 375 °C data (Fig. 7d). Water concentrations greater than model predictions could result from microfractures and cracks in the glass that decrease the effective radius of the modeled particle, while observed H_2O_{bulk} less than model predictions early in the experiments could reflect increased H_2O solubility with time as suggested by Anovitz et al., (2004). From this diffusivity and mass balance modeling, the results of which are consistent with NanoSIMS (Section 5.2.2) and two-particle mass balance

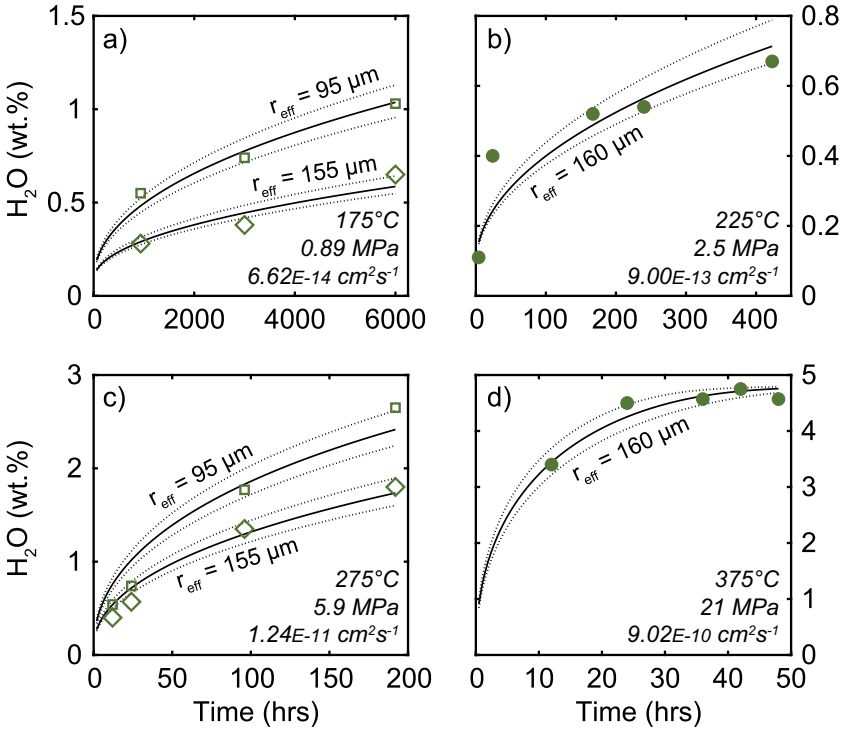

Fig. 7. Best fit curves from diffusion and mass balance models for observed H_2O concentrations at 175 °C (a), 225 °C (b), 275 °C (c), and (d). Models employ initial conditions of 0.08 wt.% H_2O and boundary conditions of 3.3 wt.% H_2O at 175 °C (a), 3.8 wt.% at 225 °C (b), 4.2 wt.% at 275 °C (c), and 4.8 wt.% at 375 °C. The H_2O concentration dependent diffusivity of Zhang and Behrens (2000) is multiplied by constant factor between 1.5–4.5 for each model. Dashed lines are 10% deviations from the effective particle radii.

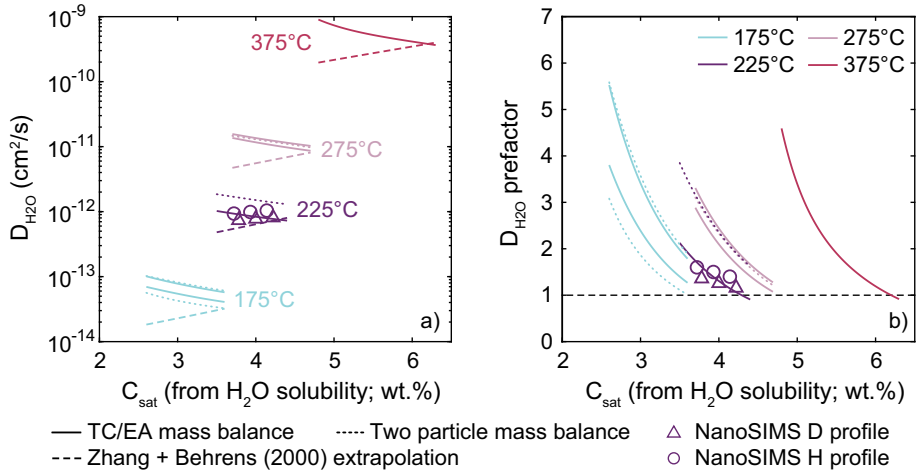

Fig. 8. C_{sat} vs. D_{H2O} on an absolute scale (a) and vs. a D_{H2O} prefactor (a scaling coefficient) that scales the high temperature extrapolations of Zhang and Behrens (2000) at the relevant P-T-X_{H2O} conditions. Diffusion and mass balance models using TC/EA data are shown with solid and dotted lines and the NanoSIMS models are shown with solid symbols. The slopes of the TC/EA based models and the NanoSIMS models differ, but routinely yield D_{H2O} values 1.5–4.5 times great than the high temperature extrapolations. Equations that define C_{sat}–D_{H2O} relationships are in Appendix F.

methods (Section 5.2.3), we conclude that D_{H2O} prefactors for our experimental temperatures are consistently 1.5–4 times greater than extrapolated from the H_2O_t, T, and P dependent diffusivity equation of Zhang and Behrens (2000).

5.2.2. Diffusion modeling of NanoSIMS D and H profiles

Raw counts of H and D from the NanoSIMS data are scaled to three different surface concentrations (3.7, 3.95, and 4.2 wt.% H_2O_t) based on the TC/EA data and solubility estimates given in Section 5.1. The results serve three primary purposes. First, it serves as a direct way to understand how H_2O solubility and diffusivity co-vary with time to produce the correct profile shape without having to be constrained by mass balance calculations and uncertainties in particle size distribution. As with the mass balance approach, changing the scaling of the profile to different values of C_{sat} for the boundary conditions requires the D_{H2O} to decrease if the H_2O solubility is increased in order to fit a diffusion profile of a given length. We observe this inverse correlation in the best fits of D_{H2O} and C_{sat} in both D and H profiles (Fig. 4b,c). The slope is different from the TC/EA diffusion and mass balance results, however, and is especially notable on the plot of absolute D_{H2O} values (Fig. 8a). The NanoSIMS modeling yields a trend that has a linear low-angle positive slope. This is because the diffusion profile length never changes in the NanoSIMS data, so only the concentration dependence of D_{H2O} causes the best fit C_{sat} value at the boundary of the model to change. This contrasts the mass balance modeling where the length scale of diffusion is allowed to vary so long as the bulk H_2O concentrations are fit. With higher modeled C_{sat}, H_2O diffusion must also be slowed (independent of the concentration dependence of D_{H2O}) in the mass balance model to reproduce the observed TC/EA measurement of H_2O_{bulk}. This results in a shallower slope to the C_{sat}-D_{H2O} relationship for the NanoSIMS data. Nevertheless, the NanoSIMS model suggests that over the most reasonable range of H_2O solubility at 225 °C (3.7–4.2 wt.% H_2O_t), D_{H2O} is less than a factor of two greater than high temperature extrapolations to hydrothermal temperatures.

The second purpose that the NanoSIMS measurements and modeling serve are that they verify the assumption that H_2O diffusion has the same functional form below the glass transition as it does at higher temperature (see dashed curve for constant D_{H2O} comparison in Fig. 4b). Other authors had previous demonstrated this using depth profiling by SIMS measured similarly shaped profiles on a scale of less than 4 μm (Anovitz et al., 2008, 2009; Riciputi et al., 2002). However, on such short length scales with complex interfacial dynamics, it has not yet been evaluated to what extent H_2O concentration dependence propagated into glass. For example, recent H_2O_t profiles measured by microRaman spectroscopy with a resolution of 1 μm from samples that are thought to have experience rapid hydrothermal temperature hydration (T ~400 °C) shows diffusion profiles that have combination of functional forms with those that are akin to the error function and those that have the functional form that arises from a concentration dependent D_{H2O} (Mitchell et al., 2018). Successful imaging of the diffusion profiles by NanoSIMS for both H and D show that even at longer durations, this behavior propagates tens of μm into glass under hydrothermal conditions.

Finally, we compare this H_2O concentration dependent model to diffusion models with constant D_{H2O} so that these results may be compared to D_{H2O} values derived for Earth surface temperatures, as these values as typically given as singular values. Using a constant D_{H2O} that is equal to half of our maximum D_{H2O} returns a profile with the form of an error function that does not fit the NanoSIMS data. However, when this profile is integrated it yields a total mass of H_2O in the glass that is within 2% of the total mass of H_2O yielded by the H_2O concentration dependent model (Fig. 4b,c). This confirms that H_2O diffusivity values con-

strained at low temperature can be directly compared to our modeled ranges of D_{H2O} values in the models (Fig. 8). The NanoSIMS data verifies that for a reasonable range of solubilities of H_2O in glass at 225 °C, the D_{H2O} in rhyolitic glasses requires the functional form of D_{H2O} at magmatic temperatures, and within an order of magnitude greater than high temperature extrapolations.

5.2.3. Two-particle D_{H2O} and H_2O solubility calculation from bulk H_2O of different particle sizes

Different particle sizes at the same experimental duration allow for mass balance calculations to predict the diffusive length of H_2O_t and its solubility in glass. For both 95 μm and 155 μm the solubility required to yield the observed H_2O_{bulk} concentrations can be calculated for every diffusion length according to Eq. (4). The modeled range of distances correspond to the diffusive lengths at which the total mass of H_2O added to the glass is equal to the product of the modeled C_{sat} and modeled distance (Fig. 9). This distance corresponds to the inflection point in the diffusion profile (which is negligibly greater than the half-fall distance, and therefore used to approximate it).

$$C_{sat} = \left(\frac{1}{m_{hyd}/m_{tot}}\right) \times \left[H_2O_{bulk} - 0.08\left(1 - \frac{m_{hyd}}{m_{tot}}\right)\right] \quad (4)$$

In this equation, C_{sat} is the H_2O solubility, m_{hyd} and m_{tot} refer to the mass of H_2O in the glass from secondary hydration and the bulk H_2O concentration. (The LSR glass has an initial concentration of 0.08 wt.% H_2O.) The measured H_2O concentration by TC/EA is given as H_2O_{bulk}. The m_{hyd} is calculated for distances from 0.1-50.0 μm in increments of 0.1 μm by assuming a density of constant density for rhyolite of 2600 kg/m^3 and that the particles are spheres. The radii are permitted to vary by 10% in these calculations in order to ensure that an analytical solution is possible. This produces a range of possible diffusive lengths constrained to ±2 μm, with the range increasing at longer durations and faster D_{H2O}. The distances at which m_{hyd} for the two particle radii and their respective H_2O_{bulk} concentrations yield the same C_{sat} reflect a non-unique, but analytically solvable combinations of H_2O solubility and D_{H2O}. The diffusion model is then run for each C_{sat} to find the D_{H2O} value that correlates with the modeled distance from the equation above. It is important to note that this mass balance model makes no assumptions about P, T, or H_2O effects on solubility. It simply reconciles D_{H2O} and H_2O solubility values that can produced the observed bulk H_2O concentrations in the TC/EA data for 2 particle sizes that have been hydrated for the same length of time under the same P-T-X_{H2O} conditions.

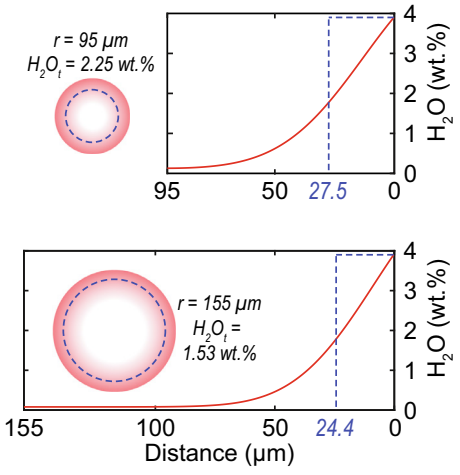

Fig. 9. Example illustrations of models from the two-particle method. For a given H_2O solubility (3.9 wt.%), there is a diffusive length that can produce the observed H_2O_{bulk} concentrations in different sized particles, which can be correlated to a specific D_{H2O}. The spherical geometry of the diffusion model yields slightly different diffusive lengths. Fitting a D_{H2O} to diffusive length in the larger particle gives a minimum estimate of D_{H2O}, in this case a prefactor of 2.57.

However, Fig. 9 shows that smaller particles will achieve longer diffusive lengths faster intrinsically because of the spherical geometry of the diffusion model. After 1010 hours of hydration, this produces a 3.1 μm difference in diffusive lengths (Fig. 9) for the necessary m_{hyd} for each particle size. Since this approximates the range of acceptable diffusive lengths by allowing a ~10% variation in the particle radii, we simply use the median value and fit D_{H2O} to this distance using the larger particle size, which makes the modeled D_{H2O} values in Fig. 8 best estimates, perhaps on the minimum side for this method.

5.2.4. H_2O diffusivity summary

The D_{H2O} results from multiple types of diffusion modeling (Fig. 8; Appendix F) are all broadly consistent, whether they come from TC/EA diffusion mass balance approaches (bulk method) or from NanoSIMS diffusion models (in situ method). The 3 types of models return diffusivity prefactors between 0.9 and 5.5 over this 200 °C temperature range for which there is scant data in the literature (Friedman and Long, 1976; Mazer et al., 1991). This indicates that extrapolations of high temperature H_2O diffusivity models perform well below the glass transition and can be extended to this sub-magmatic temperature range, but this partially depends on having accurate H_2O solubility estimates because of the H_2O concentration dependence of D_{H2O}. As we demonstrated, the high temperature extrapolations for the H_2O solubility fail to predict our observed H_2O_{bulk} concentrations.

Other factors, such as chemical composition and relative humidity, have also been shown to influence D_{H2O}. Two studies above 100 °C, but below the 400 °C give D_{H2O} higher than our modeling results (Friedman and Long, 1976; Mazer et al., 1991). Both studies, which just used optical microscopic thickness measurements, note that the D_{H2O} in rhyolitic glass appears to be somewhat composition-dependent, but only Mazer et al. (1991) calculated D_{H2O} at hydrothermal temperature for more than one composition. Using a different glass than Newberry volcano, Oregon LSR obsidian (or Icelandic Kerlingerfjöll obsidian in Friedman and Long, 1976) may have provided more overlap with the results of Mazer et al. (1991). Their results were also relative humidity-dependent (ours are at 100% humidity), so their lowest, most comparable D_{H2O}

was determined from a 60% relative humidity experiment. This may indicate that dehydration experiments at temperatures near the glass transition (e.g. Zhang and Behrens, 2000) may yield lower D_{H2O} values around 400–500 °C thereby pulling the high temperature calibration to lower values.

The D_{H2O} results presented here are bracketed by high temperature extrapolations to our experimental temperatures and two previous studies (Friedman and Long, 1976; Mazer et al., 1991; Zhang and Behrens, 2000) that ventured into the hydrothermal temperature range. The best fit D_{H2O} prefactors by any method do not exceed 5 times the extrapolation of Zhang and Behrens (2000). We note that this increase in D_{H2O} between 175 °C to 375 °C is a much smaller correction than is required to explain D_{H2O} values at Earth surface temperatures, so we propose that our model results best apply to systems with high water–rock ratios that are near or above the boiling point of H_2O.

5.3. Oxygen isotope systematics of glass hydration

Rarely reported $\delta^{18}O$ of water-in-glass analyses demonstrate that H_2O_m in glass dominates the oxygen isotope systematic of glass during hydration as it is the primary vehicle for exchange (Fig. 10). To underscore the importance of H_2O in glass on the bulk $\delta^{18}O$ composition, just 4 wt.% H_2O_t will comprise ~7% of the molar proportion of oxygen in the glass. Thus, the addition of this H_2O alone can exert a strong effect on the bulk $\delta^{18}O$ of the glass even without exchanging with the silicate matrix. For example, in both perlites and LSR obsidian at 375 °C (4.0–4.8 wt.% H_2O_{bulk}), $\delta^{18}O$ of the oxygen structurally bound in silicate ($\delta^{18}O_{sil}$) calculated from mass balance is lower than the $\delta^{18}O_{bulk}$ by approximately + 1‰ because of the high H_2O_{bulk} content (Fig. 10). Notably, meteoric waters are commonly much more depleted in $\delta^{18}O$ than our experimental water (+5.88‰ $\delta^{18}O$), so this effect is likely even more pronounced in natural systems (Seligman and Bindeman, 2019).

At our hydrothermal temperatures, H_2O_m molecules exchange their oxygen with the oxygen bound in silicate glass, so $\delta^{18}O_{wig}$ can be used to trace the progress of $\delta^{18}O$ of the bulk glass towards equilibrium. In the LSR glasses, only the 375 °C experiments and the smallest LSR at 225 °C were sufficiently long in duration to become fully hydrated and attain bulk $\delta^{18}O$ compositions in equilibrium with the hydration water, which we interpret from plateaus in bulk H_2O, $\delta^{18}O_{wig}$, and $\delta^{18}O_{bulk}$ after just 24 hours. This observation that glass exchanges silicate-bound oxygen more readily once hydrated via the diffusion of molecular H_2O through the glass explains why the perlites begin to acquire a higher bulk $\delta^{18}O$ while the anhydrous LSR obsidian is slower to change in the lower temperature experiments.

While bulk glass-water oxygen isotope equilibrium requires complete hydration, before the silicate can exchange completely with external fluid, local equilibration of $\delta^{18}O_{wig}$ with the $\delta^{18}O$ of the bulk silicate glass does not. Within this conceptual model, two equilibrium relationships – a $10^3\ln\alpha_{wig\text{-}H2O}$ and a $10^3\ln\alpha_{glass\text{-}wig}$ – together govern the $10^3\ln\alpha_{glass\text{-}H2O}$ relationship. Bulk $\delta^{18}O$ and $\delta^{18}O_{wig}$ from all experimental temperatures track the nature of oxygen isotope exchange in these two intermediate steps (Fig. 10a,b). The perlites form a nearly linear trend across all temperatures with a slope of ~1. The LSR glass, on the other hand, increase in $\delta^{18}O_{wig}$ without increasing in bulk $\delta^{18}O$ until they reach the trend of the perlites, at which point they increase along the same nearly 1:1 trajectory.

The relatively constant offset between $\delta^{18}O_{wig}$ and $\delta^{18}O_{bulk}$ (Fig. 10) can also be coarsely applied as a thermometer in glasses that have been rehydrated in excess of 2 wt.% H_2O in hydrothermal systems. We speculate that local equilibrium is quickly attained between the oxygen in molecular H_2O and oxygen in neighboring silicate bonds even when hydration is incomplete. Once the H_2O_m and the silicate glass reaches a local equilibrium with the surrounding glass, the offset between $\delta^{18}O_{wig}$ and $\delta^{18}O_{bulk}$ will be maintained during subsequent hydration as H_2O_m continues to drive

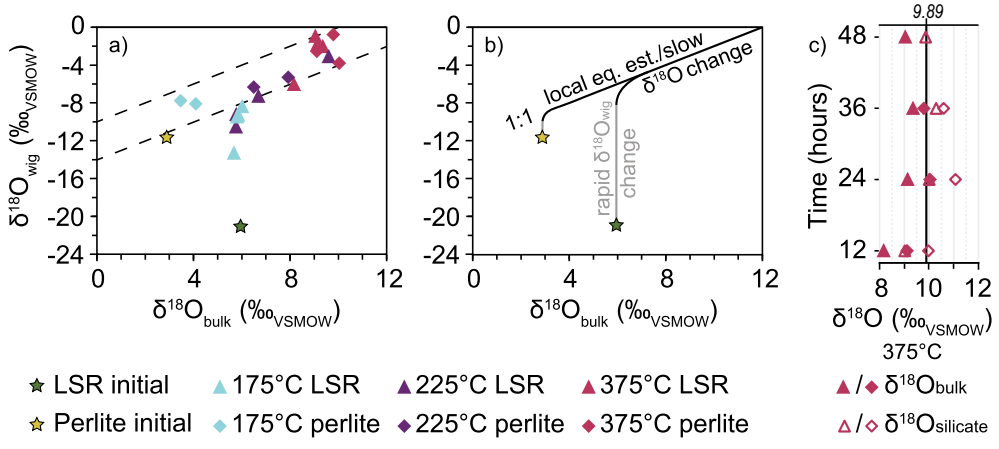

Fig. 10. The relationship between $\delta^{18}O_{bulk}$ and $\delta^{18}O_{wig}$ follows a similar trend across all temperatures (a). The high-Si perlites follow a linear trend to higher $\delta^{18}O_{bulk}$ and $\delta^{18}O_{wig}$ whereas the initially anhydrous LSR seems to increase at constant $\delta^{18}O_{bulk}$ before increasing in $\delta^{18}O_{wig}$ along the same trend as and at similar values to the perlites. This is shown schematically in (b) where $\delta^{18}O_{wig}$ rapidly equilibrates locally with the $\delta^{18}O_{bulk}$ and then both $\delta^{18}O$ parameters increase slowly together towards the equilibrium glass value. $\delta^{18}O_{bulk}$ and $\delta^{18}O_{silicate}$ straddle the predicted equilibrium value for rhyolite (9.89 ‰) with the experimental water $\delta^{18}O$ composition (c).

oxygen isotope exchange within the glass. During this process, local equilibrium should cause bulk $\delta^{18}O$ and $\delta^{18}O_{wig}$ to migrate to higher values along a trend with a slope of 1 and we observe a slope of ~1.1 (Fig. 10b). Although the $10^3\ln\alpha_{glass\text{-}wig}$ is not highly sensitive to temperature over the 175 °C to 375 °C range of these experiments relative to our conservative estimate for analytical precision (Fig. 10a), the 375 °C experimental glasses seem to have slightly smaller magnitude glass-wig fractionation (~+10‰) than the 175 °C and 225 °C glasses (~+12 to +13‰). Collectively, data from all temperatures center around a $10^3\ln\alpha_{glass\text{-}wig}$ of approximately + 12.0.

This interpretation differs somewhat from the previous studies that argue that the $\delta^{18}O_{wig}$ approximates the $\delta^{18}O$ of the hydration waters (Bindeman and Lowenstern, 2016; Hudak and Bindeman, 2018; Seligman and Bindeman, 2019). In the case of Seligman and Bindeman (2019) which use glasses hydrated at Earth surface temperatures, hydration and exchange between the silicate and the water in glass may not have proceeded rapidly, so the $\delta^{18}O_{wig}$ may simply record the $\delta^{18}O$ of the hydration waters. With hydration temperatures of ~100 °C, the lowest reported Nez Perce perlite $\delta^{18}O_{wig}$ measurement is −14.9‰ (Bindeman and Lowenstern, 2016), which approaches the modern meteoric $\delta^{18}O$ of −17‰ in thermal waters in Yellowstone (Sturchio et al., 1990). This seemed to support the idea that very little O isotope fractionation occurred between meteoric waters and the water in glass. If, as we argue in this work across all temperatures, the difference reflects rapid attainment of local O isotope equilibrium, $10^3\ln\alpha_{glass\text{-}wig}$ may instead be considered as a thermometer. Bindeman and Lowenstern (2016) and Hudak and Bindeman (2018) argue for hydration around the boiling point of H_2O at ~100 °C. Thus, the similar mean $10^3\ln\alpha_{glass\text{-}wig}$ values of 13 Yellowstone perlites of + 14.0‰ ± 1.6‰ (1σ) and 18 Crater Lake pinnacle glasses + 13.9‰ ± 2.2‰ (1σ) are an extension of our experimental results. Our experiments and these results from previous studies on natural systems represent a ~4‰ spread in $10^3\ln\alpha_{glass\text{-}wig}$ over a nearly 300 °C temperature range – from + 14‰ at 100 °C to + 10‰ at 375 °C.

6. CONCLUSIONS

We evaluated the solubility and diffusivity of H_2O in glass, and O isotope systematics of glass hydration over a hydrothermal temperature and pressure range (175–375 °C, 0.89–21 MPa). Our results on H_2O systematics in glass bridge a gap between those better studied high temperatures and Earth surface temperatures and exhibit some key similarities and differences that allow the following conclusions to be made.

(1) Our rhyolitic glasses (including both high and low silica rhyolites) yield H_2O solubility ranges of: 2.75–3.4 wt.% (175 °C, 0.89 MPa), 3.1–4.2 wt.% (225 °C, 2.55 MPa), and 4.1–5.0 wt.% (375 °C, 21 MPa), which are 1–2 wt.% higher than predicted by extrapolation from high temperature solubility models (Newman and Lowenstern, 2002; Liu et al., 2005). Pressure is likely partly responsible for the higher solubility at 375 °C and 21 MPa (no less than 4.5 wt.%) compared to 175 °C and 0.89 MPa (no greater than 3.4 wt.%). However, it cannot explain the 1–2 wt.% higher concentrations than predicted by extrapolations from high temperatures. This marks a significant difference in the H_2O solubility mechanism(s) below the glass transition. A high humidity likely also plays a role as many D_{H2O} and H_2O solubility estimates come from dehydration experiments.

(2) Low-Si rhyolite has higher H_2O solubility than high-Si rhyolite by ~0.5 wt% at 175 °C, 225 °C, and 375 °C, which may be related to the higher NBO/T ratios of high silica rhyolite.

(3) NanoSIMS measurements of D and H profiles show a "snowplow" functional form resulting from D_{H2O} dependence on H_2O content, as is also observed in silicate melts at magmatic temperatures.

(4) Modeled D_{H2O} values plotted against 1/T exhibit an approximate, linear Arrhenius relationship with D_{H2O} values up to 5.5 times greater than extrapolation of higher T experiments (Zhang and Behrens, 2000), depending on the chosen solubility for the relevant P-T-X_{H2O} conditions. The continuation of high temperature D_{H2O} relationships, however, does depend on having high H_2O solubility.

(5) Oxygen isotopes are exchanged in two steps: first via H_2O_m diffusion into glass, then by local exchange with silicate. We observe that initially anhydrous glasses show limited exchange with bulk glass $\delta^{18}O$ (except for at 375 °C), but initially hydrous perlites begin to exchange with added H_2O and change bulk $\delta^{18}O$ immediately. The $\delta^{18}O_{wig}$ approaches local equilibrium with the $\delta^{18}O_{glass}$ rapidly (within weeks at 225 °C and within days at 375 °C) and subsequent back-diffusion of lighter $\delta^{18}O$ H_2O_m out of the glass drives $\delta^{18}O_{wig}$ and $\delta^{18}O_{glass}$ towards higher $\delta^{18}O$ values in equilibrium with the external water.

(6) This isotope diffusion–reaction process appears to be achieved quickly in the 375 °C experiments where complete hydration occurs after 2 days. The $\delta^{18}O_{bulk}$ of 9-10‰ and a $\delta^{18}O_{wig}$ of ~−1‰ indicate $10^3\ln\alpha_{glass\text{-}wig}$ is 10-11‰. The equilibrium $10^3\ln\alpha_{glass\text{-}wig}$ seems to be locally achieved rapidly at all temperatures and $10^3\ln\alpha_{glass\text{-}wig}$ is ~14‰ and ~10‰ between 100 °C to 375 °C.

(7) Using our methods, we cannot detect kinetic isotope fractionation of D relative to H. This, along with the evidence from O isotopes indicate that D/H isotope exchange via H_2O_m, appears to be the main isotope exchange mechanism between silicate glass and water.

Declaration of Competing Interest

The authors declare that they have no known competing financial interests or personal relationships that could have appeared to influence the work reported in this paper.

ACKNOWLEDGEMENTS

We thank J. Palandri for assistance with $\delta^{18}O$ analyses, J. Donovan and J. Chouinard for assistance on the EPMA, A. Schauer for analyzing our water for δD and $\delta^{18}O$, and Y. Guan for collecting the NanoSIMS data and for his assistance with methods. We appreciate T. Giachetti for allowing us to use his particle size analyzer and J. Wiejaczka and K. Trafton for their help operating it. We are also grateful to L. Anovitz and five anonymous reviewers for their helpful comments which greatly improved this manuscript. This work was supported by NSF grants EAR 1822977 and EAR 1447447, and a Graduate Student Research Grant from Geological Society of America.

APPENDIX A. SUPPLEMENTARY MATERIAL

Supplementary data to this article can be found online at https://doi.org/10.1016/j.gca.2020.06.009.

REFERENCES

Anovitz L. M., Cole D. R. and Fayek M. (2008) Mechanisms of rhyolitic glass hydration below the glass transition. *Am. Mineral.* **93**, 1166–1178.

Anovitz L. M., Cole D. R. and Riciputi L. R. (2009) Low-temperature isotopic exchange in obsidian: Implications for diffusive mechanisms. *Geochim. Cosmochim. Acta* **73**, 3795–3806.

Anovitz L. M., Elam J. M., Riciputi L. R. and Cole D. R. (2004) Isothermal time-series determination of the rate of diffusion of water in Pachuca obsidian. *Archaeometry* **2**, 301–326.

von Aulock F. W., Nichols A. R. L., Kennedy B. M. and Oze C. (2013) Timescales of texture development in a cooling lava dome. *Geochim. Cosmochim. Acta* **114**, 72–80.

Befus K. S., Watkins J., Gardner J. E., Richard D., Befus K. M., Miller N. R. and Dingwell D. B. (2015) Spherulites as in-situ recorders of thermal history in lava flows. *Geology* **43**, 647–650.

Behrens H. and Nowak M. (1997) The mechanisms of water diffusion in polymerized silicate melts. *Contrib. Mineral. Petrol.* **126**, 377–385.

Behrens H., Zhang Y., Leschik M., Wiedenbeck M., Heide G. and Frischat G. H. (2007) Molecular H_2O as carrier for oxygen diffusion in hydrous silicate melts. *Earth Planet. Sci. Lett.* **254**, 69–76.

Bindeman I. N. and Lowenstern J. B. (2016) Low-δD hydration rinds in Yellowstone perlites record rapid syneruptive hydration during glaical and interglacial conditions. *Contrib. Mineral. Petrol.*, 171.

Breitkreuz C. (2013) Spherulites and lithophysae-200 years of investigation on high-temperature crystallization domains in silica-rich volcanic rocks. *Bull. Volcanol.* **75**, 1–16.

Canavan R. R., Carrapa B., Clementz M. T., Quade J., DeCelles P. G. and Schoenbohm L. M. (2014) Early cenozoic uplift of the Puna plateau, central andes, based on stable isotope paleoaltimetry of hydrated volcanic glass. *Geology* **42**, 447–450.

Cassel E. J. and Breecker D. O. (2017) Long-term stability of hydrogen isotope ratios in hydrated volcanic glass. *Geochim. Cosmochim. Acta* **200**, 67–86.

Cassel E. J., Breecker D. O., Henry C. D., Larson T. E. and Stockli D. F. (2014) Profile of a paleo-orogen: High topography across the present-day Basin and Range from 40 to 23 Ma. *Geology* **42**, 1007–1010.

Cassel E. J., Graham S. A. and Chamberlain C. P. (2009) Cenozoic tectonic and topographic evolution of the northern Sierra Nevada, California, through stable isotope paleoaltimetry in volcanic glass. *Geology* **37**, 547–550.

Cassel E. J., Graham S. A., Chamberlain C. P. and Henry C. D. (2012) Early Cenozoic topography, morphology, and tectonics of the northern Sierra Nevada and western Basin and Range. *Geosphere* **8**, 229–249.

Cerling T. E., Brown F. H. and Bowman J. R. (1985) Low-temperature alteration of volcanic glass: hydration, Na, K, ^{18}O and Ar mobility. *Chem. Geol.* **52**, 281–293.

Colwyn D. A. and Hren M. T. (2019) An abrupt decrease in Southern Hemisphere terrestrial temperature during the Eocene-Oligocene transition. *Earth Planet. Sci. Lett.* **512**, 227–235.

Cullen J. T., Hurwitz S., Barnes J. D., Lassiter J. C., Penniston-Dorland S., Kasemann S. A. and Thordsen J. J. (2019) Temperature-dependent variations in mineralogy, major element chemistry and the stable isotopes of boron, lithium and chlorine resulting from hydration of rhyolite: Constraints from hydrothermal experiments at 150 to 350 °C and 25 MPa. *Geochim. Cosmochim. Acta* **261**, 269–287.

Delaney J. R. and Karsten J. L. (1982) Ion microprobe studies of water in silicate melts: temperature-dependent water diffusion in obsidian. *Earth Planet. Sci. Lett.* **59**, 420–428.

Dettinger M. P. and Quade J. (2015) Testing the analytical protocols and calibration of volcanic glass for the reconstruction of hydrogen isotopes in paleoprecipitation. *Mem. Geol. Soc. Am.* **212**, 261–276.

Dingwell D. B. (1995) Relaxation in silicate melts: some applications. In *Reviews in Mineralogy and Geochemistry: Structure, Dynamics and Properties of Silicate Melts*, pp. 21–66.

Dingwell D. B. and Webb S. L. (1990) Relaxation in silicate melts. *Eur. J. Mineral.*, 427–449.

Eichelberger J. C. and Westrich H. R. (1981) Magmatic volatiles in explosive rhyolitic eruptions. *Geophys. Res. Lett.* **8**, 757–760.

Friedman I., Gleason J., Sheppard R. A. and Gude A. J. (1993a) Deuterium fractionation as water diffuses into silicic volcanic ash. In *Climate Change in Continental Isotopic Records* (eds. P. K. Swart, K. C. Lohmann, J. Mckenzie and S. Savin), pp. 321–323.

Friedman I., Gleason J. and Warden A. (1993b) Ancient climate from deuterium content of water in volcanic glass. In *Climate Change in Continental Isotopic Records* (eds. P. K. Swart, K. C. Lohmann, J. Mckenzie and S. Savin), pp. 309–319.

Friedman I. and Long W. (1976) Hydration Rate of Obsidian. *Science* **191**, 347–352.

Friedman I. and Obradovich J. (1981) Obsidian hydration dating of volcanic events. *Quat. Res.* **16**, 37–47.

Friedman I. and Smith R. L. (1960) A new dating method using obsidian: Part I, the development of the method. *Am. Antiq.* **25**, 476–493.

Friedman I., Smith R. L. and Long W. D. (1966) Hydration of natural glass and formation of perlite. *Geol. Soc. Am. Bull.* **77**, 323–328.

Gardner J. E., Befus K. S., Watkins J., Hesse M. and Miller N. (2012) Compositional gradients surrounding spherulites in obsidian and their relationship to spherulite growth and lava cooling. *Bull. Volcanol.* **74**, 1865–1879.

Giachetti T., Gonnermann H. M., Gardner J. E., Shea T. and Gouldstone A. (2015) Discriminating secondary from magmatic water in rhyolitic matrix-glass of volcanic pyroclasts using thermogravimetric analysis. *Geochim. Cosmochim. Acta* **148**, 457–476.

Giachetti T., Hudak M. R., Shea T., Bindeman I. N. and Hoxsie E. C. (2020) D/H ratios and H_2O contents record degassing and rehydration history of rhyolitic magma and pyroclasts. *Earth Planet. Sci. Lett.*, 530.

Hess K. U. and Dingwell D. B. (1996) Viscosities of hydrous leucogranitic melts: a non-Arrhenian model. *Am. Mineral.* **81**, 1297–1300.

Horita J. and Wesolowski D. J. (1994) Liquid-vapor fractionation of oxygen and hydrogen isotopes of water from the freezing to the critical temperature. *Geochim. Cosmochim. Acta* **58**, 3425–3437.

Hudak M. R. and Bindeman I. N. (2018) Conditions of pinnacle formation and glass hydration in cooling ignimbrite sheets from H and O isotope systematics at Crater Lake and the Valley of Ten Thousand Smokes. *Earth Planet. Sci. Lett.* **500**, 56–66.

Jackson L. J., Horton B. K., Beate B. O., Bright J. and Breecker D. O. (2019) Testing stable isotope paleoaltimetry with Quaternary volcanic glasses from the Ecuadorian Andes. *Geology* **47**, 411–414.

Keating G. N. (2005) The role of water in cooling ignimbrites. *J. Volcanol. Geotherm. Res.* **142**, 145–171.

Lapham K. E., Holloway J. R. and Delaney J. R. (1984) Diffusion of H_2O and D_2O in obsidian at elevated temperatures and pressures. *J. Non. Cryst. Solids* **67**, 179–191.

Liritzis I. and Laskaris N. (2011) Fifty years of obsidian hydration dating in archaeology. *J. Non. Cryst. Solids* **357**, 2011–2023.

Liu Y., Zhang Y. and Behrens H. (2005) Solubility of H_2O in rhyolitic melts at low pressures and a new empirical model for mixed H_2O-CO_2 solubility in rhyolitic melts. *J. Volcanol. Geotherm. Res.* **143**, 219–235.

Loewen M. W., Bindeman I. N. and Melnik O. E. (2017) Eruption mechanisms and short duration of large rhyolitic lava flows of Yellowstone. *Earth Planet. Sci. Lett.* **458**, 80–91.

Manga M. (1998) Orientation distribution of microlites in obsidian. *J. Volcanol. Geotherm. Res.* **86**, 107–115.

Martin E., Bindeman I., Balan E., Palandri J., Seligman A. and Villemant B. (2017) Hydrogen isotope determination by TC/EA technique in application to volcanic glass as a window into secondary hydration. *J. Volcanol. Geotherm. Res.*.

Mazer J. J., Stevenson C. M., Ebert W. L. and Bates J. K. (1991) The experimental hydration of obsidian as a function of relative humidty and temperature. *Am. Antiq.* **56**, 504–513.

Michels J. W., Tsong I. S. T. and Nelson C. M. (1983) Obsidian dating and east African Archeology. *Science* **219**, 361–366.

Mitchell S. J., McIntosh I. M., Houghton B. F., Carey R. J. and Shea T. (2018) Dynamics of a powerful deep submarine eruption recorded in H_2O contents and speciation in rhyolitic glass: The 2012 Havre eruption. *Earth Planet. Sci. Lett.* **494**, 135–147.

Newman S. and Lowenstern J. B. (2002) Volatile Calc: a silicate melt – H2O – CO2 solution model written in Visual Basic for excel. *Comput. Geosci.* **28**, 597–604.

Ni H. and Zhang Y. (2008) H_2O diffusion models in rhyolitic melt with new high pressure data. *Chem. Geol.* **250**, 68–78.

Nolan G. S. and Bindeman I. N. (2013) Experimental investigation of rates and mechanisms of isotope exchange (O, H) between volcanic ash and isotopically-labeled water. *Geochim. Cosmochim. Acta* **111**, 5–27.

O'Neil J. R. and Taylor H. P. (1967) The oxygen isotope and cation exchange chemistry of feldspars. *Am. Mineral.* **52**, 1414–1437.

Randolph-Flagg N., Breen S., Hernandez A., Manga M. and Self S. (2017) Evenly spaced columns in the Bishop Tuff (California, USA) as relicts of hydrothermal cooling. *Geology* **45**, 1015–1018.

Riciputi L. R., Elam J. M., Anovitz L. M. and Cole D. R. (2002) Obsidian diffusion dating by secondary ion mass spectrometry: A test using results from mound 65, Chalco, Mexico. *J. Archaeol. Sci.* **29**, 1055–1075.

Rogers A. K. and Duke D. (2011) An archaeologically validated protocol for computing obsidian hydration rates from laboratory data. *J. Archaeol. Sci.* **38**, 1340–1345.

Roskosz M., Deloule E., Ingrin J., Depecker C., Laporte D., Merkel S., Remusat L. and Leroux H. (2018) Kinetic D/H fractionation during hydration and dehydration of silicate glasses, melts and nominally anhydrous minerals. *Geochim. Cosmochim. Acta* **233**, 14–32.

Ryan A. G., Russell J. K., Nichols A. R. L., Hess K.-U. and Porritt L. A. (2015) Experiments and models on H_2O retrograde solubility in volcanic systems. *Am. Mineral.* **100**, 774–786.

Seligman A. N., Bindeman I., Van Eaton A. and Hoblitt R. (2018) Isotopic insights into the degassing and secondary hydration of volcanic glass from the 1980 eruptions of Mount St. Helens. *Bull. Volcanol.*, 80.

Seligman A. N. and Bindeman I. N. (2019) The $\delta^{18}O$ of primary and secondary waters in hydrous volcanic glass. *J. Volcanol. Geotherm. Res.* **371**, 72–85.

Seligman A. N., Bindeman I. N., Watkins J. M. and Ross A. M. (2016) Water in volcanic glass: From volcanic degassing to secondary hydration. *Geochim. Cosmochim. Acta* **191**, 216–238.

Sharp Z. D., Gibbons J. A., Maltsev O., Atudorei V., Pack A., Sengupta S., Shock E. L. and Knauth L. P. (2016) A calibration of the triple oxygen isotope fractionation in the SiO_2-H_2O system and applications to natural samples. *Geochim. Cosmochim. Acta* **186**, 105–119.

Shelby J. E. (1977) Molecular diffusion and solubility of hydrogen isotopes in vitreous silica. *J. Appl. Phys.* **48**, 3387–3394.

Sparks R. S. J. (1978) The dynamics of bubble formation and growth in magmas: A review and analysis. *J. Volcanol. Geotherm. Res.* **3**, 1–37.

Stevenson C. M., Ladefoged T. N. and Novak S. W. (2013) Prehistoric settlement chronology on Rapa Nui, Chile: Obsidian hydration dating using infrared photoacoustic spectroscopy. *J. Archaeol. Sci.* **40**, 3021–3030.

Stroncik N. A. and Schmincke H. U. (2001) Evolution of palagonite: Crystallization, chemical changes, and element budget. *Geochemistry, Geophys. Geosystems* **2**.

Sturchio N. C., Keith T. E. C. and Muehlenbachs K. (1990) Oxygen and carbon isotope ratios of hydrothermal minerals from Yellowstone drill cores. *J. Volcanol. Geotherm. Res.* **40**, 23–37.

Thien B. M. J., Kosakowski G. and Kulik D. A. (2015) Differential alteration of basaltic lava flows and hyaloclastites in Icelandic hydrothermal systems. *Geotherm. Energy* **3**, 11.

Trafton K., Giachetti T. and Kruse H. (2019) Pumice: The size dependency of density. *American Geophysical Union Fall Meeting San Francisco, CA*.

Watkins J. M., Manga M. and Depaolo D. J. (2012) Bubble geobarometry: A record of pressure changes, degassing, and regassing at Mono Craters, California. *Geology*, 699–702.

Watkins J., Manga M., Huber C. and Martin M. (2009) Diffusion-controlled spherulite growth in obsidian inferred from H_2O concentration profiles. *Contrib. Mineral. Petrol.* **157**, 163–172.

Wilding M. C., Webb S. L. and Dingwell D. B. (1995) Evaluation of a relaxation geospeedometer for volcanic glasses. *Chem. Geol.* **125**, 137–148.

Wilding M., Dingwell D., Batiza R. and Wilson L. (2000) Cooling rates of hyaloclastites: Applications of relaxation geospeedometry to undersea volcanic deposits. *Bull. Volcanol.* **61**, 527–536.

Xu Z. and Zhang Y. (2002) Quench rates in air, water, and liquid nitrogen, and inference of temperature in volcanic eruption columns. *Earth Planet. Sci. Lett.* **200**, 315–330.

Yokoyama T., Okumura S. and Nakashima S. (2008) Hydration of rhyolitic glass during weathering as characterized by IR microspectroscopy. *Geochim. Cosmochim. Acta* **72**, 117–125.

Zhang Y. and Behrens H. (2000) H_2O diffusion in rhyolitic melts and glasses. *Chem. Geol.* **169**, 243–262.

Zhang Y., Jenkins J. and Xu Z. (1997) Kinetics of the reaction $H_2O + O \rightarrow 2OH$ in rhyolitic glasses upon cooling: Geospeedometry and comparison with glass transition. *Geochim. Cosmochim. Acta* **61**, 2167–2173.

Zhang Y., Stolper E. M. and Wasserburg G. J. (1991) Diffusion of water in rhyolitic glasses. *Geochim. Cosmochim. Acta* **55**, 441–456.

Zhang Y., Xu Z., Zhu M. and Wang H. (2007) Silicate melt properties and volcanic eruptions. *Rev. Geophys.* **45**, 1–27.

Associate editor: Lawrence M. Anovitz